https://doi.org/10.5194/tc-2021-157
Preprint. Discussion started: 7 June 2021

The Cryosphere Discussions
Open Access
EGU

Antarctic snow-covered sea ice topography derivation from TanDEM-X using polarimetric SAR interferometry

Lanqing Huang[1], Georg Fischer[2], and Irena Hajnsek[1,2]

[1]Institute of Environmental Engineering, Swiss Federal Institute of Technology in Zurich (ETH), 8093 Zürich, Switzerland.
[2]Microwaves and Radar Institute, German Aerospace Center (DLR), Wessling 82234, Germany.

Correspondence: Lanqing Huang (huang@ifu.baug.ethz.ch)

Abstract.

Single-pass interferometric synthetic aperture radar (InSAR) enables the possibility for sea ice topographic retrieval despite the inherent dynamics of sea ice. InSAR digital elevation models (DEM) are measuring the radar scattering center height. The height bias induced by the penetration of electromagnetic waves into snow and ice leads to inaccuracies of the InSAR DEM, especially for multi-year sea ice with snow cover. In this study, an elevation difference between the satellite-measured InSAR DEM and the airborne-measured optical DEM is observed from a coordinated campaign over the western Weddell Sea in Antarctica. The objective is to correct the penetration bias and generate a precise sea ice topographic map from the single-pass InSAR data. With the potential of retrieving sea ice geophysical information by the polarimetric-interferometry (Pol-InSAR) technique, a two-layer plus volume model is proposed to represent the sea ice vertical structure and its scattering mechanisms. Furthermore, a simplified version of the model is derived, to allow its inversion with limited a priori knowledge, which is then applied to a topographic retrieval scheme. The model-retrieved performance is validated with the optical DEM of the sea ice topography, showing an excellent performance with root-mean-square error as low as $0.22\,\mathrm{m}$. The experiments are performed across four polarizations: HH, VV, Pauli-1 (HH+VV), and Pauli-2 (HH-VV), indicating the polarization-independent volume scattering property of the sea ice in the investigated co-polarized data.

1 Introduction

Sea ice topography is the elevation of the ice volume including the snow cover above the sea level. The sea ice topographic height on spatial scales of meters is dominated by ice ridges, shear zones, and hummocks, due to the forces from ocean winds and currents, together with the blocking effects from the coast and islands (Rampal et al., 2009).

Characterizing sea ice topography is valuable for various geophysical parameters over polar oceans. For instance, the atmospheric drag coefficient over sea ice is an important topography-dependent parameter to understand the interaction at the ice-atmosphere boundary (Garbrecht et al., 2002; Castellani et al., 2014). Interpretation of sea ice topography is also essential in estimating sea ice thickness. Tucker III and Govoni (1981) observed a square-root relation between the ridge height and thickness, which is further validated by additional in situ observations in (Tucker et al., 1984). A sea ice thickness retrieval using the sea ice topographic height and the square-root relation function was conducted in the Arctic region, performing a

https://doi.org/10.5194/tc-2021-157
Preprint. Discussion started: 7 June 2021


The Cryosphere Discussions
Open Access
EGU

maximum $\pm 2\,\mathrm{m}$ difference between the observed and predicted ice thickness (Petty et al., 2016). In Antarctica, Toyota et al. (2011) demonstrated that the mean ice thickness of snow-covered ice is highly correlated with the sea ice topography; this raises the possibility of estimating ice thickness in east Antarctica. Nowadays, precise characterization of sea ice topography is a topic of active research.

The sea ice topography can be measured by various instruments, such as laser altimeters (Dierking, 1995; Schutz et al., 2005; Abdalati et al., 2010; Farrell et al., 2011) and stereo cameras using photogrammetric techniques (Divine et al., 2016; Dotson and Arvesen., 2012, updated 2014). However, the major limitation of above measurements is the small spatial coverage. Synthetic aperture radar (SAR) achieves a good balance between wide-spatial coverage and high resolution and becomes an invaluable asset for monitoring polar regions thanks to its ability to provide all-weather, day/night imagery. Interferometric SAR (InSAR) offers an opportunity to estimate surface height from two or more image pairs (Rodriguez and Martin, 1992). However, due to the inherent dynamics of sea ice, it is impossible to derive height over sea ice from a single SAR sensor by repeat-pass interferometry, because of its temporal decorrelation. Only single-pass interferometry offers the possibility to characterize the sea ice topography (Dierking et al., 2017). TanDEM-X is a single-pass SAR interferometer developed by the German Aerospace Center (DLR) (Krieger et al., 2007) and is providing high resolution co-registered single-look complex data on a global scale. With its single-pass nature combined with the flexibility in both spatial and temporal baseline, height retrieval over sea ice becomes promising despite the dynamic nature of sea ice. Dierking et al. (2017) demonstrated the theoretical potential of generating sea ice height from the single-pass InSAR data and discussed the factors that may impede the accuracy of the retrieval in practice. From TanDEM-X InSAR acquisitions, the derivation of topography over snow-free multi-year sea ice was demonstrated and verified with laser and photogrammetric measurements (Yitayew et al., 2018). Until now, the InSAR technique has become one of the most promising tools for sea ice height estimation.

However, a digital elevation model (DEM) derived with InSAR is affected by the penetration of microwave signals into dry, frozen snow and ice. In fact, an InSAR DEM is actually a measurement of the radar scattering center height, which can be below the surface due to the microwave penetration. This height bias leads to inaccuracies of InSAR DEMs, especially for multi-year sea ice with snow cover. The microwave penetration into snow and ice is described by the electromagnetic penetration depth δ_p. It is determined by the signal extinction coefficient σ in units of decibels per unit length (e.g., $\mathrm{dB/cm}$, $\mathrm{dB/m}$), which indicates the decrease of the signal strength inside the medium. The total electromagnetic loss in a medium consists of both scattering and absorption losses. Scattering loss results from particles of different relative permittivity embedded in a host medium. The absorption loss depends on the imaginary part of the relative permittivity ϵ'' (Hallikainen and Winebrenner, 1992). Larger δ_p are found in multi-year ice due to the smaller ϵ'' attributed by the deficient brine compared to first-year ice. For sensors operating at X-band, experimental penetration depth for sea ice ranges from about $0.05\,\mathrm{m}$ to $1\,\mathrm{m}$, depending on the sea ice type, salinity, and temperature (Hallikainen and Winebrenner, 1992). Snow on top causes a greater range of δ_p due to the high sensitivity of ϵ'' to water content. Dry, fine grained snow can have δ_p values up to hundreds of wavelengths (Cloude, 2010).

In this study, we observed an elevation discrepancy between the InSAR DEM and the photogrammetric DEMs which were acquired from a coordinated campaign (Nghiem et al., 2018) conducted with DLR's TanDEM-X satellite and the NASA Icebridge aircraft over the sea ice in the western Weddell Sea, Antarctica. The elevation difference reveals the necessity to

https://doi.org/10.5194/tc-2021-157
Preprint. Discussion started: 7 June 2021

consider the penetration depth δ_p when retrieving sea ice topography from the InSAR imagery. The objective of this study is to compensate the penetration depth and thereby obtain an accurate sea ice topographic map with wide spatial coverage. Note that the studied area is snow-covered sea ice, therefore the term “sea ice topographic height", throughout the paper, refers to the sea ice height including snow depth above local sea level.

The estimation of the penetration depth of InSAR signals can be inferred from the interferometric volume decorrelation, which is one of the key components of the interferometric coherence. The volume decorrelation is caused by backscatter contributions from different depths and can be derived from the integral of an assumed vertical scattering distribution function with finite or infinite depth. The investigation of vertical distribution functions for various scattering processes, known as the polarimetric-interferometry SAR (Pol-InSAR) technique (Papathanassiou and Cloude, 2001), is widely applied in retrieving geophysical parameters from several natural volumes, such as forest (Kugler et al., 2015), agriculture (Joerg et al., 2018), ice sheets (Fischer et al., 2018), and glaciers (Sharma et al., 2012). To the best of our knowledge, only a few studies have assessed the potential of retrieving geophysical information by means of the Pol-InSAR technique for sea ice. Dierking et al. (2017) estimated the penetration depth into sea ice volume under the assumption of uniform lossy volume with an exponential vertical function. However, for snow-covered sea ice, the scattering effects from the snow volume and sub-layers such as the snow-ice interface also need to be considered. In order to achieve an effective estimation of penetration depth, factors including the physical structures, the electromagnetic properties, as well as the scattering mechanisms within the sea ice volume need to be understood and properly modelled.

Sea ice can be modelled as a multi-layer structure behaving as a mixture of surface, volume, and surface-volume interaction scattering in microwave remote sensing (Nghiem et al., 1995a, b; Albert et al., 2012). When the electromagnetic waves penetrate the volume, the inhomogeneous materials inside the volume (i.e., a mixture of constituents such as brine, ice, and air bubbles) excite the occurrence of volume scattering (Nghiem et al., 1995a). Besides, the surface conditions such as rough interfaces, hummocks, and snow cover can increase the surface scattering at the rough air-snow interface, snow-ice interface, and ice-water interface (Nghiem et al., 1990). The surface-volume interaction component (Albert et al., 2012) further complicates the overall scattering mechanisms.

Huang and Hajnsek (2021) investigated the X-band SAR polarimetric behaviour for several types of ice over the western Weddell Sea, including new ice, thin ice, thick ice, and deformed ice with ridges. For the area covered by the thick and deformed ice, an empirically inverse relation between the elevation difference and the co-polarimetric coherence was observed, indicating that the SAR polarimetry carries significant topographic information (Huang and Hajnsek, 2021). Based on the previous work, this study offers a further understanding of the elevation difference between the InSAR DEM and the optical DEM from investigating the polarimetric behaviours and exploiting the interferometric volume decorrelation. A novel model is proposed to characterize the scattering processes, and an inversion scheme is developed for height retrieval. Therefore, compared to the previous work, this study is a crucial step forward towards developing an advanced algorithm for sea ice topographic estimation.

In this study, enlightened by the multi-layer sea ice models utilized for electromagnetic simulation in (Nghiem et al., 1990, 1995a, b; Albert et al., 2012), a two-layer plus volume model is proposed to relate interferometric coherence to extinction

https://doi.org/10.5194/tc-2021-157
Preprint. Discussion started: 7 June 2021

coefficients, layer depths, and layer-to-volume ratio for layers. The model sensitivity to the variation of several parameters is analyzed, and the model accuracy is assessed with various baseline configurations. With the goal to develop and invert the model for sea ice topographic retrieval, the proposed theoretical model is further simplified by reducing the required amount of input parameters. An inversion scheme for topographic retrieval using both the theoretical and simplified model is established. The sea ice topographic height is retrieved in different polarizations over around $50\,\mathrm{km} \times 18\,\mathrm{km}$ area in the west Weddell Sea. The model-retrieved DEM is validated against a photogrammetric DEM, proving the effectiveness of the proposed model and the inversion scheme.

The organization of the paper is as follows. Section 2 introduces the basic concepts of Pol-InSAR technique. Section 3 introduces the data sets and the preprocessing procedures. A two-layer theoretical model and a simplified model are proposed in Section 4. A model inversion scheme is developed in Section 5 to achieve the sea ice topographic retrieval. In Section 6, the proposed methodology is applied to the study area, and the experimental results are discussed. The conclusion is drawn in Section 7.

2 Basic concepts

For single-pass systems, the complex interferometric coherence $\tilde{\gamma}_{\mathrm{InSAR}}$ can be decomposed into a product of terms (Cloude, 2010)

$$\tilde{\gamma}_{\mathrm{InSAR}} = e^{i\phi_0}\gamma_{\mathrm{s}}\gamma_{\mathrm{SNR}}\tilde{\gamma}_v \tag{1}$$

where ϕ_0 is the topographic phase. γ_{s} is the baseline or surface decorrelation which depends on the nature of the surface scattering; it can always be removed by employing range spectral filtering and thus is set equal to 1 in this study. γ_{SNR} denotes decorrelation due to additive noise in the signals. $\tilde{\gamma}_v$ refers to the complex volume decorrelation.

In the case of pure surface scattering, the interferometric coherence can be approximated to be $\tilde{\gamma}_{\mathrm{InSAR}} \approx e^{i\phi_0}\gamma_{\mathrm{SNR}}$, assuming that volume scattering can be neglected (i.e., $\tilde{\gamma}_v \approx 1$). γ_{SNR} only contributes to the magnitude of $\tilde{\gamma}_{\mathrm{InSAR}}$; therefore the InSAR scattering phase center, denoted as $\angle\tilde{\gamma}_{\mathrm{InSAR}}$, purely contains the information of topographic phase ϕ_0. In this case, $\angle\tilde{\gamma}_{\mathrm{InSAR}}$ can be directly converted to topographic height.

However, in the case of snow-covered multi-year sea ice, when the electromagnetic waves penetrate into the snow and ice volume, the inhomogeneous materials inside the volume can excite volume scattering (Nghiem et al., 1995a). Then, the volume decorrelation in Eq. (1) can not be approximated to be 1. Both the topographic phase ϕ_0 and the complex $\tilde{\gamma}_v$ contribute to the InSAR scattering phase center $\angle\tilde{\gamma}_{\mathrm{InSAR}}$. In this case, in order to obtain an accurate topographic phase ϕ_0, $\tilde{\gamma}_v$ has to be properly modelled and estimated. The main contribution of this paper is the development of a novel two-layer plus volume model (Section 4) for $\tilde{\gamma}_v$, which is applied for an improved sea ice topographic retrieval.

The volume decorrelation $\tilde{\gamma}_v$ depends on the vertical distribution of backscattering $\sigma_v(z)$ (Cloude, 2010)

$$\tilde{\gamma}_v = \frac{\int_0^D \sigma_v(z) e^{i\kappa_{z\_\mathrm{vol}} z} dz}{\int_0^D \sigma_v(z) dz} \tag{2}$$

https://doi.org/10.5194/tc-2021-157
Preprint. Discussion started: 7 June 2021

where the surface is located at $z = 0$, D is the thickness of volume, and κ_{z_vol} is the vertical wavenumber in the volume (Sharma et al., 2012; Dall, 2007)

$$\kappa_{z\_\mathrm{vol}} = \frac{2\pi}{h_{a\_\mathrm{vol}}} = \frac{2\pi}{h_a \frac{\sqrt{\epsilon' - \sin^2\theta}}{\epsilon' \cos\theta}} \tag{3}$$

where h_a is the height of ambiguity in free space, h_{a_vol} is the height of ambiguity in the volume, θ is the incidence angle (in the air), and ϵ' is the dielectric constant of volume and is assumed to be 2.8 (Dierking et al., 2017) throughout this study. Note that the height of ambiguity is defined as the height difference that generates an interferometric phase change of 2π. The height of ambiguity is inversely proportional to the perpendicular baseline (Leinss, 2015)

$$h_a = \frac{\lambda H \tan\theta}{2b_\perp} \tag{4}$$

where λ is wavelength, H is orbit height, and $b_\perp$ is the effective perpendicular baseline of TanDEM-X bi-static mode.

In Eq. (2), $\tilde{\gamma}_v$ can be estimated by choosing an appropriate vertical structural function $\sigma_v(z)$ and a suitable InSAR baseline configuration using Eq. (3) and Eq. (4), and then be substituted into Eq. (1) to obtain the topography of snow-covered sea ice.

3 Data sets and preprocessing

This section introduces the campaign, the study area, and the data sets. The InSAR processing and its performance are also described.

3.1 Campaign and study area

A coordinated campaign between the NASA's Operation IceBridge (OIB) airborne mission and the DLR's TanDEM-X satellite mission was successfully conducted on Oct 29, 2017, named as OIB/TanDEM-X Coordinated Science Campaign (OTASC) (Nghiem et al., 2018). The OTASC data have been successfully used in investigating the topography of iceberg (Dammann et al., 2019) and sea ice (Huang and Hajnsek, 2021).

As presented in Fig. 1(a), the study area is located in the western Weddell Sea, near the east coast of the Antarctic Peninsula. The TanDEM-X SAR intensity image of the study area is shown in Fig. 1(b) where the optical images and the transect of photogrammetric measurements of the sea ice topography are superimposed. From the optical images taken by the airborne digital camera, it is visible that the study region is covered by thick and deformed ice with ridges and has a snow cover on top.

3.2 TanDEM-X

The German TanDEM-X mission is a single-pass SAR interferometer operating at X-band at a wavelength of $3\,\mathrm{cm}$. With nearly no temporal gap, TanDEM-X collects two images of the same footprint seen from slightly different viewing angles to generate the topography of the Earth's surface (Krieger et al., 2007). The studied InSAR images are acquired at UTC 23:41 Oct 29, 2017 in a bi-static mode. The InSAR pair is a Co-registered Single look Slant range Complex (CoSSC) product with

https://doi.org/10.5194/tc-2021-157
Preprint. Discussion started: 7 June 2021

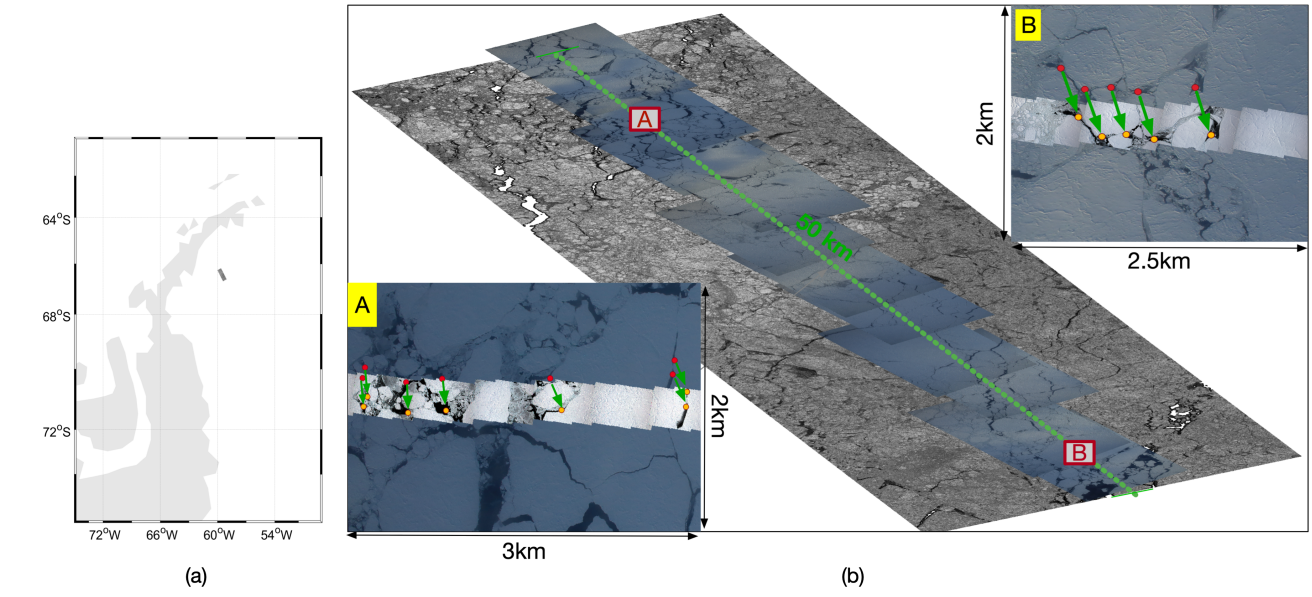

Figure 1. (a) Geo-location of the study area (the grey rectangular). (b) Merge of the SAR intensity image in HH polarization and the airborne DMS digital camera images. The green dashed line indicates the $50\,\mathrm{km}$ transect of the DMS DEM data. Sub-image A and sub-image B are zoom-in of area A and area B with small-scale DMS images (acquired at around UTC 17:50) superimposed on the large-scale DMS images (acquired at around UTC 22:05). The red and yellow dots denote the selected reference pairs from the large- and small-scale DMS image, respectively. The green arrow denotes the 'shift-vector' which is used for data co-registration.

dual-polarization (HH and VV) in StripMap mode. The incidence angle of the scene center is $34.8°$, and the pixel spacing is $0.9\,\mathrm{m} \times 2.7\,\mathrm{m}$ in range and azimuth. The effective perpendicular baseline $b_\perp$ is $175.7\,\mathrm{m}$ and the along-track baseline b_{al} is $201.9\,\mathrm{m}$. The height of ambiguity h_a is $32.5\,\mathrm{m}$.

3.3 DMS

The digital mapping system (DMS) is one of the OIB airborne instruments which is acquiring a set of different data from a digital camera system. This study uses the airborne DMS digital camera images (Dominguez, 2010, updated 2018) and the airborne DMS DEMs (Dotson and Arvesen., 2012, updated 2014).

The DMS digital camera captures natural color and panchromatic imagery, hereby named as DMS images for conciseness. The DMS images are geolocated and orthorectified, with a high spatial resolution varying from $0.015\,\mathrm{m}$ to $2.5\,\mathrm{m}$ depending on the flight altitude (Dominguez, 2010, updated 2018). Two types of photography: large- and small-scale DMS images, are obtained during the airborne overflights. The large-scale DMS images over the study area were acquired from UTC 22:01 to 22:07 on Oct 29, 2017, each with a spatial coverage of around $5.8\,\mathrm{km}$ by $8.8\,\mathrm{km}$, shown in Fig. 1(b). The small-scale DMS images covering the study area were captured from UTC 17:45 to 17:52 on Oct 29, 2017, and each file is about $400\,\mathrm{m}$ by $400\,\mathrm{m}$

https://doi.org/10.5194/tc-2021-157
Preprint. Discussion started: 7 June 2021

spatial coverage. The transect of small-scale DMS images is shown in the green dashed line in Fig. 1(b) and enlarged in Fig. 1(b) sub-image A and B, where the details of sea ice structure become visible.

The DMS DEM is generated from the small-scale DMS images by a photogrammetric technique and is calibrated with the LIDAR altimetry measurements (Dotson and Arvesen., 2012, updated 2014). For the snow-covered sea ice, the DMS DEM measures sea ice height including snow depth. The data are acquired along a $50\,\mathrm{km}$ transect with a swath width of $400\,\mathrm{m}$ (Dotson and Arvesen., 2012, updated 2014). Each DMS DEM has a $400\,\mathrm{m}$ by $400\,\mathrm{m}$ spatial coverage and $40 \times 40\,\mathrm{cm}$ spatial resolution. Note that the temporal gap between the DMS DEM and TanDEM-X SAR acquisitions is about 6 hours.

In this study, the DMS DEMs are further processed following four steps: reprojection, mosaicing, geocoding, and calibration. First, the DMS DEMs are reprojected from Antarctic Polar Stereographic to WGS84 spatial reference. The second step is the mosaicing of adjacent files into the $50\,\mathrm{km}$ transect with a swath width of $400\,\mathrm{m}$. Third, using the GAMMA software, the merged DMS DEM is geocoded into the SAR coordinate system and re-sampled into the same resolution (i.e., $\sim 10 \times 10\,\mathrm{m}$ in range and azimuth) as the multilook TanDEM-X image. Finally, as the DMS DEMs are given in meters above the WGS-84 ellipsoid, the sea ice topographic height in this paper is calibrated to the local sea level by selecting the water-surface reference from DMS images.

3.4 Data co-registration

Due to the inherent dynamics of sea ice and the temporal gap between the DMS DEM and TanDEM-X acquisitions, data co-registration is employed to cancel the shift and thereby ensure a valid pixel-by-pixel comparison in the experiments.

The large- and small-scale DMS images, although acquired at different time, both clearly reveal the shape and size of ice floes; therefore they are used to match identical sea ice features, referred to as 'reference pair' in the following. The co-registration is performed by tracking the movement of the selected reference pairs. Specifically, we manually label several pairs of distinguishable features (i.e. the ice floes of a particular shape, or leads) on both the large-scale DMS image and the small-scale DMS image, which is acquired about 4 hours 15 minutes later. By extracting the two geo-locations of the reference pair, a 'shift-velocity vector' can be derived in the unit of meter per hour in both azimuth and range directions in the radar coordinate. As the temporal difference between the DMS DEM and the SAR acquisition is 5 hours $49 - 56$ minutes, the shift-distance can be estimated, assuming constant sea ice motion, based on the 'shift-velocity vector' and utilized for the co-registration.

In the studied image, the focus is the $50\,\mathrm{km}$ transect (green dashed line in Fig. 1(b)) overlaid by the DMS flight track. The transect is divided into 50 segments, and each segment contains 1×100 pixels in range and azimuth corresponding to about $1\mathrm{km}$ length. For each segment, several reference pairs are selected and labelled (marked in red and yellow dots on the large- and small- scale DMS images, respectively, in Fig. 1(b) sub-image A and B). The 'shift-velocity vectors' are calculated and annotated by the green arrows. Then, data co-registration is conducted by multiplying the derived 'shift-velocity vector' with the temporal gap for each segment respectively. The co-registered results of all segments are confirmed by the visualization of the DMS images and the SAR images. The segments which still contain residual mis-coregistration induced by the sea ice non-linear movement or rotation are excluded and will not be used in the following experiments.

https://doi.org/10.5194/tc-2021-157
Preprint. Discussion started: 7 June 2021


The Cryosphere Discussions

3.5 InSAR processing

The TanDEM-X InSAR pair is generated as the CoSSC products; thus, the co-registration and common spectral band filtering in range and azimuth have already been processed (Duque et al., 2012). The remaining InSAR processing includes interferogram generation, flat earth removal, interferogram filtering, low-coherence area mask, phase unwrapping, and phase-to-height conversion. All steps are carried out with the GAMMA software. A 4×12 window in azimuth and slant range is applied in the processing, corresponding to about $10\,\mathrm{m} \times 10\,\mathrm{m}$ spatial size.

In single-pass interferometry, two simultaneous observations, denoted as s_1 and s_2, are made. The complex interferogram γ and interferometric phase ϕ_γ can be calculated as (Cloude, 2010)

$$\gamma = s_1 s_2^* \tag{5}$$

$$\phi_\gamma = \arg\{s_1 s_2^*\} \tag{6}$$

where symbol $(^*)$ denotes the complex conjugate.

However, for scatterers lying in a plane, $\Delta z = 0$, the phase gradient can be related to the effective perpendicular baseline $b_\perp$ (Cloude, 2010). It is called the flat-earth component of the interferometric phase, a high-frequency component of the phase signal, which can be removed by the process of flat-earth removal using the GAMMA software. Then, the adaptive filter (Goldstein and Werner, 1998) is applied to the flat-earth removed interferogram.

The interferometric coherence is a measurement of signal correlation between two acquisitions. It is calculated by (Cloude, 2010)

$$\tilde{\gamma}_{\mathrm{InSAR}} = \frac{< s_1 s_2^* >}{\sqrt{< s_1 s_1^* >< s_2 s_2^* >}} \tag{7}$$

where the symbol $< . >$ denotes an ensemble average. Here, a 4×12 window in azimuth and slant range is applied to estimate $\tilde{\gamma}_{\mathrm{InSAR}}$ for four polarizations: HH, VV, Pauli-1 (HH+VV), and Pauli-2 (HH-VV). Areas with $|\tilde{\gamma}_{\mathrm{InSAR}}|$ less than 0.3 are masked out and will not be considered in the following processing. For conciseness, only the interferometric coherence in HH polarization is shown in Fig. 2(a). The $|\tilde{\gamma}_{\mathrm{InSAR}}|$ histograms for the four polarizations are plotted in Fig. 3, from which the interferometric decorrelation varying among different polarizations can be observed. $|\tilde{\gamma}_{\mathrm{InSAR}}|$ for HH and VV polarizations shows small differences, mainly lying in a range of $0.6 - 0.8$. The Pauli-1 polarization has the highest $|\tilde{\gamma}_{\mathrm{InSAR}}|$ of $0.7 - 0.8$ with a small distribution; whereas the Pauli-2 polarization shows the lowest values with a wider spread of the coherence, which is mainly due to the lower signal-to-noise ratio (SNR). The observed interferometric decorrelation indicates the necessity to consider the volume scattering contributing to the InSAR decorrelation.

The phase unwrapping and the phase-to-height conversion (Goldstein et al., 1988; Rodriguez and Martin, 1992) are also carried out with the GAMMA software. The InSAR DEM h_{InSAR} is derived for the four polarizations. Again, only the HH polarization is shown in Fig. 2(b) for conciseness. The comparison between h_{InSAR} for the four polarizations and the DMS

https://doi.org/10.5194/tc-2021-157
Preprint. Discussion started: 7 June 2021

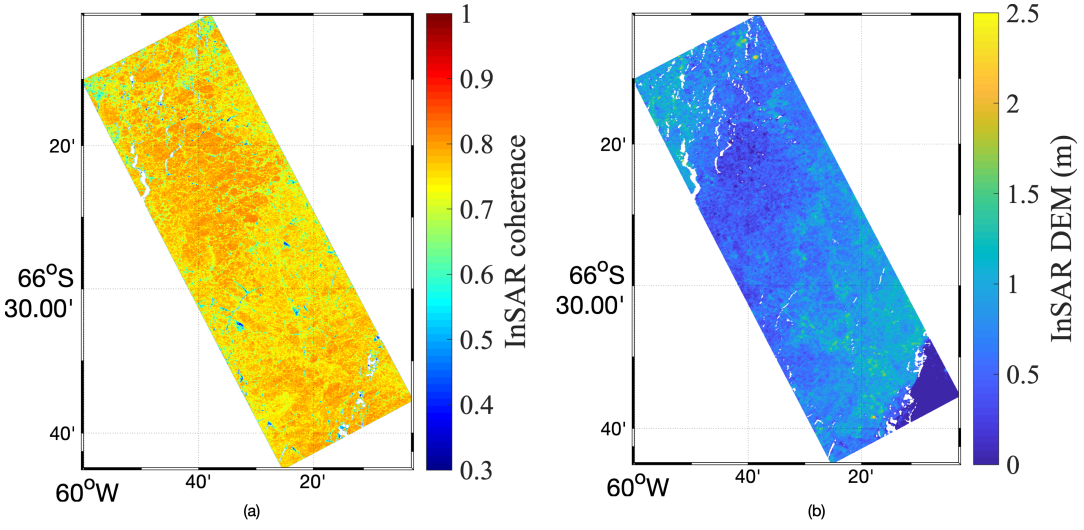

Figure 2. (a) Magnitude of the interferometric coherence $|\tilde{\gamma}_{\mathrm{InSAR}}|$ and (b) InSAR DEM h_{InSAR} for HH polarization.

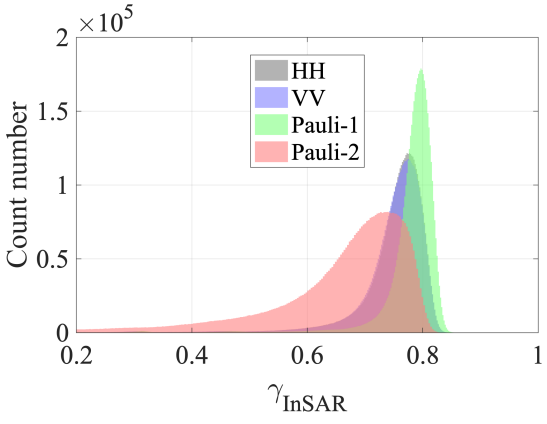

Figure 3. Magnitude of the interferometric coherence $|\tilde{\gamma}_{\mathrm{InSAR}}|$.

https://doi.org/10.5194/tc-2021-157
Preprint. Discussion started: 7 June 2021

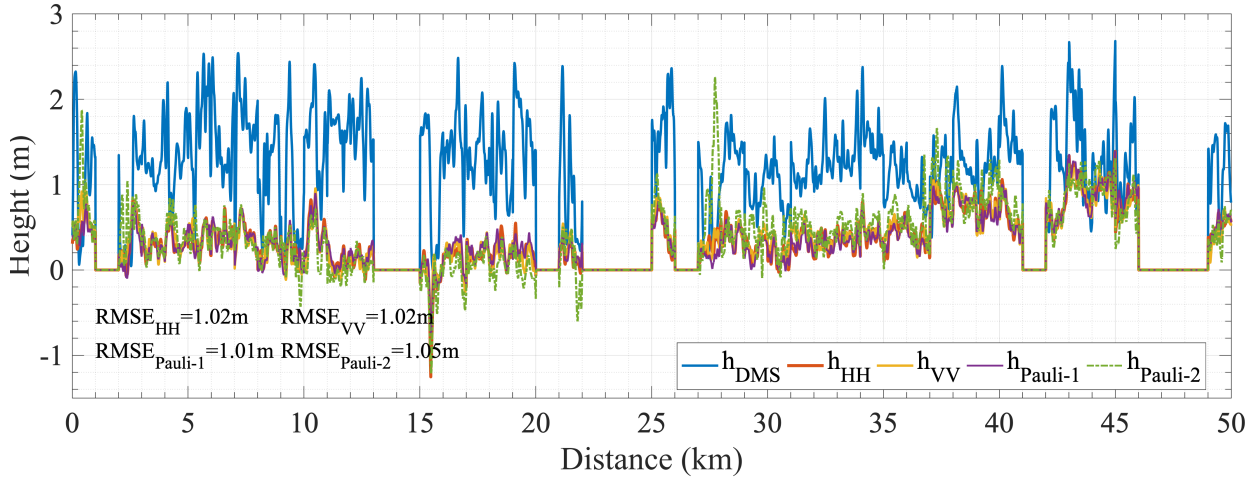

Figure 4. The InSAR-derived height profiles (h_{InSAR}) and the DMS DEM (h_{DMS}). The excluded segments due to mis-coregistration are set to be $0\,\mathrm{m}$ height.

DEM h_{DMS} along the flight track (the green dashed line in Fig. 1) is shown in Fig. 4, with a maximum elevation difference around $2\,\mathrm{m}$. The differences of h_{InSAR} across the four polarizations are illustrated in Fig. 5, where the height differences mostly lie in the range of $-0.5\,\mathrm{m}$ to $0.5\,\mathrm{m}$. The InSAR-derived heights from Pauli-1 and HH polarizations reveal the most similar values; while Pauli-2 and HH polarizations show the largest height difference, which is accordant with the wider spread distribution of InSAR coherence in Pauli-2 channel (see Fig. 3). The root-mean-square errors $RMSE$ between h_{InSAR} and h_{DMS} are averaged to be $\sim 1.03\,\mathrm{m}$ for the four polarizations, indicating that the penetration of electromagnetic wave into snow and ice volume should be properly considered and corrected for sea ice topographic retrieval, at least for the deformed thick ice with snow cover in this study.

It can be summarized that both the interferometric decorrelation and the elevation difference between the InSAR DEM and the DMS DEM highlight the necessity for developing an appropriate method aimed at an accurate sea ice topography retrieval.

4 Model development

This section proposes a two-layer plus volume model to describe the interferometric coherence of sea ice. Simulations are performed to analyze the model sensitivity and accuracy by varying parameter sets and baseline configurations. In a separate step, the model is further simplified to fulfill the practical propose of deriving the sea ice topography.

https://doi.org/10.5194/tc-2021-157
Preprint. Discussion started: 7 June 2021

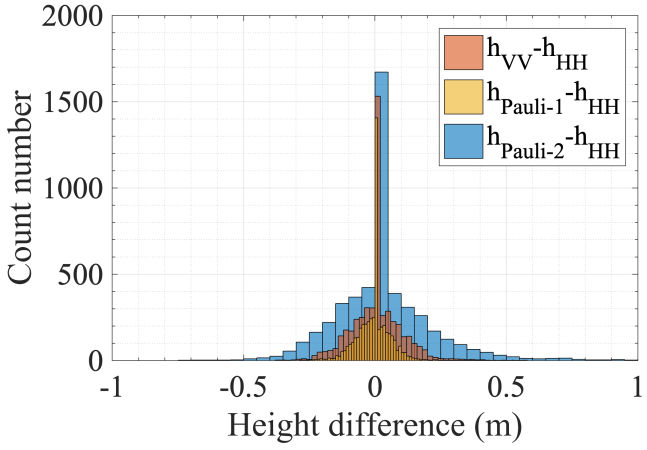

Figure 5. Height difference between the InSAR-derived height (h_{InSAR}) in HH polarization and other three polarizations.

4.1 Removal of SNR decorrelation

A formalism including the signal-to-noise ratio (SNR) decorrelation, the wave-scattering (volume) decorrelation, and other components has been introduced in Eq. (1) in Section 2. The magnitude of the $\tilde{\gamma}_{\mathrm{InSAR}}$ can be corrected for γ_{SNR} and γ_{s} by rewriting Eq. (1) as

$$\tilde{\gamma}_{\mathrm{InSAR}'} = \frac{\tilde{\gamma}_{\mathrm{InSAR}}}{\gamma_{\mathrm{s}}\gamma_{\mathrm{SNR}}} = e^{i\phi_0}\tilde{\gamma}_v \tag{8}$$

where $\tilde{\gamma}_{\mathrm{InSAR}'}$ is the SNR-removed interferometric coherence. γ_{SNR} can be estimated as a function of SNR (Cloude, 2010)

$$\gamma_{\mathrm{SNR}} = \frac{SNR}{1+SNR} = \frac{S(\mathrm{dB}) - N(\mathrm{dB})}{1 + S(\mathrm{dB}) - N(\mathrm{dB})} \tag{9}$$

with S being the backscattering signal and N being the noise floor (i.e., the noise equivalent sigma zero (NESZ)). The standard TanDEM-X products provide a set of polynomial coefficients which describe the NESZ pattern for each polarization along the range direction (Eineder et al., 2008). For the studied InSAR pair, which contains the TDX and TSX images, the NESZ patterns are shown in Fig. 6(a). $\mathrm{NESZ}_{\mathrm{HH}}$ and $\mathrm{NESZ}_{\mathrm{VV}}$ are the values along the range direction for the TDX and TSX images in HH and VV polarization, respectively. For Pauli-1 and Pauli-2, the NESZ pattern is estimated by averaging $\mathrm{NESZ}_{\mathrm{HH}}$ and $\mathrm{NESZ}_{\mathrm{VV}}$. According to Eq. (9), the γ_{SNR} histograms for the four polarizations are calculated and shown in Fig. 6(b), which indicate the importance to correctly account for γ_{SNR}.

4.2 Composite coherence model for sea ice

The sea ice volume has been modelled as a multi-layer structure in microwave remote sensing (Nghiem et al., 1990; Albert et al., 2012). We propose a two-layer plus volume model considering snow cover, ice volume, and sea water, illustrated in Fig.

https://doi.org/10.5194/tc-2021-157
Preprint. Discussion started: 7 June 2021

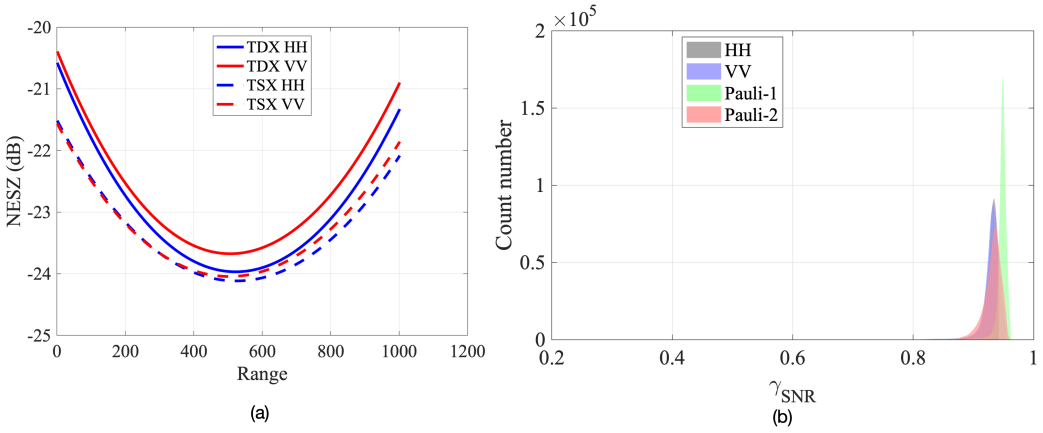

Figure 6. (a) Noise pattern both polarizations (i.e., HH and VV) and both satellites (i.e., TDX and TSX). (b) SNR-coherence γ_{SNR} for the four polarizations.

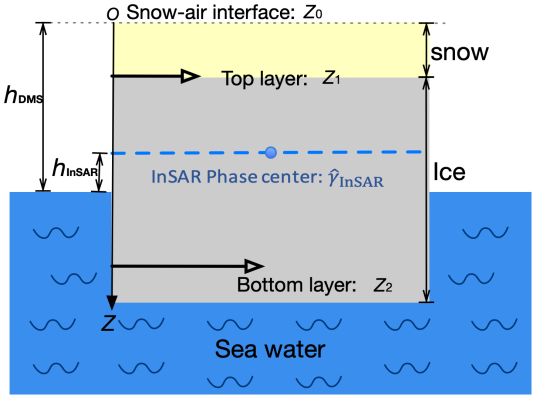

Figure 7. Schematic of the proposed two-layer plus volume model for sea ice.

7, behaving as a mix of surface and volume scattering under radar illumination. The uppermost surface (i.e., snow-air interface) is located at z_0.

Surface scattering is considered to originate mainly from two interfaces, named as the top layer and the bottom layer, respectively. The top layer located at z_1 is the snow-ice interface, which can induce significant surface scattering due to a slush layer with high permittivity (Hallikainen and Winebrenner, 1992). The position of the bottom layer (z_2) could be somewhere inside of ice volume or at the ice-water interface. The vertical distributions of the top and bottom surface can be modelled as two Dirac delta functions at the specific layer position, with an additional parameter, defined as the layer-to-volume scattering ratio (Fischer et al., 2018). Hence, the surface scattering component in the context of interferometry is modelled as (Fischer

https://doi.org/10.5194/tc-2021-157
Preprint. Discussion started: 7 June 2021

et al., 2018)

$$\tilde{\gamma}_{\text{Layer}} = e^{i\phi_0} \frac{m_1 e^{i\kappa_{z\_\text{vol}} z_1} + m_2 e^{i\kappa_{z\_\text{vol}} z_2}}{m_1 + m_2} \tag{10}$$

where m_1 and m_2 are the layer-to-volume ratio of the top and bottom layer, respectively.

The volume scattering is attributed to the constituents in the snow (from z_0 to z_1) and ice (from z_1 to z_2) volumes (Hallikainen and Winebrenner, 1992). Both volumes are assumed to be uniform volumes, which means that the scattering coefficient per unit volume and the extinction coefficient σ have no spatial variation. In this case, the vertical structure function $\sigma_v(z)$ becomes exponential. The $\tilde{\gamma}_v$ for a uniform volume model can be formulated as (Papathanassiou and Cloude, 2001)

$$\tilde{\gamma}_v(\sigma, D) = \frac{\int_0^D e^{\frac{2\sigma z}{\cos\theta_r}} e^{i\kappa_{z\_\text{vol}} z} dz}{\int_0^D e^{\frac{2\sigma z}{\cos\theta_r}} dz} \tag{11}$$

where θ_r is the incidence angle in the volume, σ is the constant extinction coefficient, and D is the volume thickness. The corresponding volume coherences can be derived according to Eq. (11), denoted as $\tilde{\gamma}_v(\sigma_1, z_{01})$ and $\tilde{\gamma}_v(\sigma_2, z_{12})$ for the snow and ice volumes, respectively, where $z_{01} = z_0 - z_1$ is the thickness of the snow volume and $z_{12} = z_1 - z_2$ is the thickness of the ice volume.

For the overall two-layer plus volume model, the interferometric coherence can be given as a combination of volume and surface effects which are described by Eq. (10) and Eq. (11), respectively. As represented in Fig. 7, if we set z_0 as the origin of the coordinate and thus to be 0, z_1 and z_2 being the position of two layers with negative values, the composite interferometric coherence is postulated to be

$$\begin{aligned} &\tilde{\gamma}_{\text{InSAR}'} \\ &= e^{i\phi_0} \frac{\alpha\tilde{\gamma}_v(\sigma_1, z_{01}) + e^{i\phi_1}(1-\alpha)\tilde{\gamma}_v(\sigma_2, z_{12}) + m_1 e^{i\phi_1} + m_2 e^{i\phi_2}}{1 + m_1 + m_2} \\ &= e^{i\phi_0} \tilde{\gamma}_{\text{mod\_T}}(\sigma_1, \sigma_2, \alpha, m_1, m_2, z_1, z_2) \end{aligned} \tag{12}$$

where $\phi_1 = \kappa_{z\_\text{vol}} z_1$, $\phi_2 = \kappa_{z\_\text{vol}} z_2$, σ_1 and σ_2 are extinction coefficients of snow and ice volume, respectively, in the unit of Np/m. Note that $\sigma(\text{dB/m}) = \frac{10}{\ln 10}\sigma(\text{Np/m}) = 4.343\,\sigma(\text{Np/m})$. The volume coherences of snow $\tilde{\gamma}_{\text{v}}(\sigma_1, z_{01})$ and ice $\tilde{\gamma}_{\text{v}}(\sigma_2, z_{12})$ can be obtained according to Eq. (11). Weight parameter α ($\in [0, 1]$) represents the proportion of the snow volume scattering in the combined (snow and ice) volume scattering.

4.3 Analysis of model sensitivity

The prediction of $\tilde{\gamma}_{\text{mod\_T}}$ from the proposed two-layer plus volume model by Eq. (12) requires seven parameters: extinction coefficients σ_1, σ_2 (dB/m), layer-to-volume ratio m_1, m_2, layer-position z_1, z_2 (m), and weight parameter α. However, it is impossible to estimate all unknowns based on only two observables: the phase and magnitude of $\tilde{\gamma}_{\text{InSAR}'}$. Therefore, the necessary simplicity in terms of model parameters should be considered for the model inversion, which is addressed in Sections 4.5 and 5.

https://doi.org/10.5194/tc-2021-157
Preprint. Discussion started: 7 June 2021

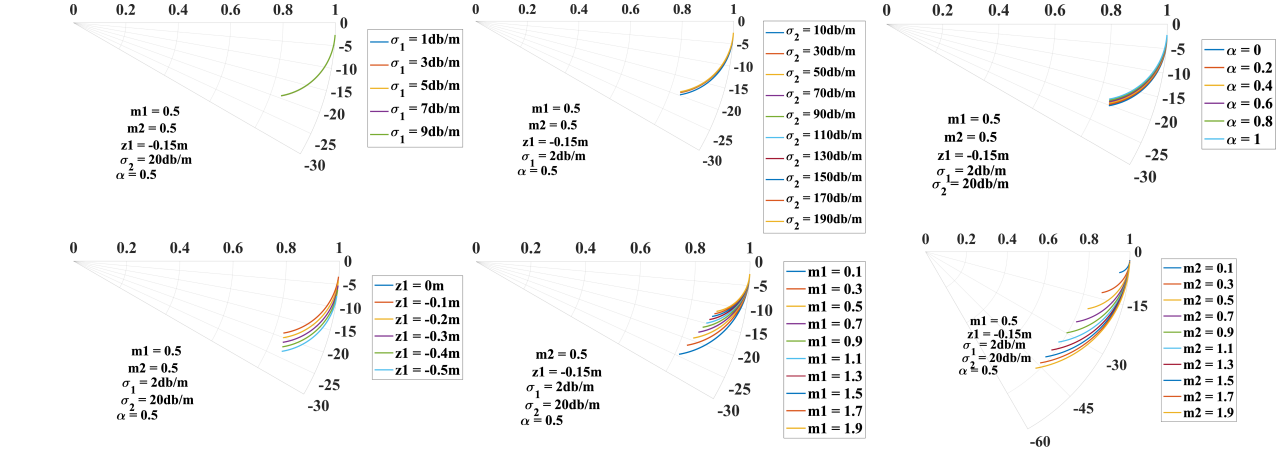

Figure 8. Simulation of $\tilde{\gamma}_{\mathrm{mod\_T}}$ for the proposed model by varying (a) snow extinction σ_1, (b) ice extinction σ_2, (c) weight parameter α, (d) top-layer position z_1, (e) top-layer layer-to-volume ratio m_1, and (f) bottom-layer layer-to-volume ratio m_2.

The simulation aims at reducing the number of unknowns of the model by selecting the parameters which induce minor variance of $\tilde{\gamma}_{\mathrm{mod\_T}}$. The sensitivity of $\tilde{\gamma}_{\mathrm{mod\_T}}$ to various parameters is presented in Fig. 8. It shows the complex $\tilde{\gamma}_{\mathrm{mod\_T}}$ as a function of the ice-volume height ($h_v = z_1 - z_2$, ranging from 0 to $-5\,\mathrm{m}$) by varying only one parameter and keeping the others constant. The κ_z for the studied image is calculated to be $0.28\,\mathrm{rad/m}$ by Eq. (3).

Figure 8(a) and Fig. 8(b) show the loci obtained for $\alpha = 0.5$, $m_1 = 0.5$, $m_2 = 0.5$, $z_1 = -0.15\,\mathrm{m}$ with increasing σ_1 and σ_2, respectively. The snow extinction coefficient σ_1 depends on the electromagnetic wave's frequency, snow temperature, volumetric water content, snow density, and the shape of the ice particles. At $10\,\mathrm{GHz}$ frequency, the snow extinction coefficient was measured to be $1-10\,\mathrm{db/m}$ (Haykin et al., 1994). This range of values is considered for σ_1 in Fig. 8(a). Sea ice consists of pure ice, brine inclusions, and air bubbles. The properties and geometry of these constituents together with the environmental conditions influence the sea ice extinction coefficient σ_2. Experimental values of sea ice extinction coefficient at $10\,\mathrm{GHz}$ are given in (Hallikainen and Winebrenner, 1992), ranging from 10 to $200\,\mathrm{dB/m}$ covering different types of sea ice (cf. Fig. 8(b)). Figure 8(c) shows the loci obtained for $m_1 = 0.5$, $m_2 = 0.5$, $\sigma_1 = 2\,\mathrm{dB/m}$, and $\sigma_2 = 20\,\mathrm{dB/m}$ with α varying from 0 to 1.

As illustrated in Fig. 8(a)-(c), the simulated $\tilde{\gamma}_{\mathrm{mod\_T}}$ is marginally sensitive to the variance of σ_1, σ_2, and α, suggesting the possibility to fix them as constant so as to reduce the model complexity. This marginal sensitivity of both volume contributions can be understood by looking at their complex contributions to Eq. (12). The snow volume $\tilde{\gamma}_{\mathrm{v}}(\sigma_1, z_{01})$, with its small vertical extent of $15\,\mathrm{cm}$ and across the range of low extinction coefficients, has an individual coherence magnitude close to unity with its phase center at about -6 to $-7\,\mathrm{cm}$. Therefore, it acts almost as a constant contribution, which is additionally located close to the Dirac delta of the top layer $m_1 e^{i\phi_1}$ in the complex unit circle. Similarly, the ice volume $\tilde{\gamma}_{\mathrm{v}}(\sigma_2, z_{12})$ has an individual coherence magnitude of almost unity and a phase center between -15 to $-33\,\mathrm{cm}$ for the investigated range of ice extinction coefficients. Therefore, its effects have a limited variablity and are also more or less aligned with the top layer. These observations are only valid for the investigated κ_{z_vol} and might differ for baselines larger than usual for TanDEM-X.

https://doi.org/10.5194/tc-2021-157
Preprint. Discussion started: 7 June 2021

Figure 8(d) shows the loci obtained for $\alpha = 0.5$, $m_1 = 0.5$, $m_2 = 0.5$, $\sigma_1 = 2\,\mathrm{dB/m}$, and $\sigma_2 = 20\,\mathrm{dB/m}$ with snow depth z_1 varying from 0 to $-0.5\,\mathrm{m}$. The influence of the snow depth on $\tilde{\gamma}_{\mathrm{mod\_T}}$ is not negligible. One way to address this is by using a priori knowledge from external sources. With fixed values of α, σ_1, σ_2, and z_1, the loci with different m_1 and m_2 values are illustrated in Fig. 8(e) and Fig. 8(f), respectively. The simulated $\tilde{\gamma}_{\mathrm{mod\_T}}$ shows sensitivity to the variance of the layer-to-volume ratio of the top layer in Fig. 8(e). However, estimations of m_1 from observations are challenging due to the insufficient measurements of the sea ice condition over the study area. Therefore, m_1 is approximately set to be a constant value in the proposed theoretical model. A simplified model, which avoids estimating m_1, will be introduced in Section 4.5. For the layer-to-volume ratio of the bottom layer, m_2 induces significant variance to $\tilde{\gamma}_{\mathrm{mod\_T}}$, indicating m_2 as the most deterministic parameter which should be properly estimated to ensure the accuracy of model inversion.

4.4 Assessment of model accuracy

The observed interferometric coherence $\tilde{\gamma}_{\mathrm{InSAR}'}$ can be biased by a residual non-volumetric decorrelation component γ_{res}, even after accounting for γ_{s} and γ_{SNR} by means of Eq. (8). γ_{res} can induce further errors when performing the model inversion for height estimation (Kugler et al., 2015). Therefore, based on Eq. (12), this potential error term is considered as

$$\tilde{\gamma}_{\mathrm{InSAR}'} = e^{i\phi_0}\tilde{\gamma}_{\mathrm{mod\_T}}\gamma_{\mathrm{res}} \tag{13}$$

In the inversion, the height uncertainty depends on the magnitude of $\tilde{\gamma}_{\mathrm{InSAR}'}$ (i.e., $|\tilde{\gamma}_{\mathrm{InSAR}'}|$) and the InSAR baseline configuration (i.e., κ_{z_vol}) . In this subsection, a Monte-Carlo simulation is performed to assess the height uncertainty with various $|\tilde{\gamma}_{\mathrm{InSAR}'}|$ and κ_{z_vol} values. The estimation of coherence itself has a variance due to its stochastic nature and the number of looks (i.e. the size of the coherence estimation window). In other words, the estimation accuracy of $\tilde{\gamma}_{\mathrm{InSAR}'}$ depends on the standard deviation of its magnitude and phase which are defined by the statistical distribution and the number of looks for multilook SAR data (Kugler et al., 2015; Touzi and Lopes, 1996; Lopes et al., 1992). The statistical distribution of coherence magnitude and phase can be given as follows.

The probability density function (pdf) of coherence magnitude γ is obtained as (Touzi and Lopes, 1996)

$$P(\gamma) = 2(N-1)(1-D^2)^N\gamma(1-\gamma^2)^{N-2}F(N,N;1,D^2\gamma^2) \tag{14}$$

where N is the number of looks, F is a hypergeometric function, and D is the expectation value of coherence level.

The pdf of sample coherence phase ϕ follows (Lopes et al., 1992)

$$\begin{aligned} P(\phi) = &\frac{(1-D^2)^N}{2\pi}[{}_3F_2(1,N,N;0.5,N;D^2\cos^2(\phi-\beta)) + k'D\cos(\phi-\beta))\times{}_3F_2(1.5,N+0.5,N+0.5;\\ &1.5,N+0.5;D^2\cos^2(\phi-\beta))] \end{aligned} \tag{15}$$

where $k' = \Gamma(0.5)\Gamma(N+0.5)/\Gamma(N)$, ${}_3F_2$ is a generalized hypergeometric function, and β is the mean phase difference.

The simulation is a four-step procedure. First, the complex value of $\tilde{\gamma}_{\mathrm{mod\_T}}$ is calculated for the designed two-layer plus volume model with specific parameters $(\sigma_1, \sigma_2, \alpha, m_1, m_2, z_1, z_2)$ and a given κ_{z_vol}. The surface phase ϕ_0 is assumed to be 0. Second, $\tilde{\gamma}_{\mathrm{sim}}$ is obtained by $\tilde{\gamma}_{\mathrm{sim}} = \tilde{\gamma}_{\mathrm{mod\_T}}\gamma_{\mathrm{res}}$ with $\gamma_{\mathrm{res}} = 0.98$ (according to (Kugler et al., 2015)). Next, a set of

https://doi.org/10.5194/tc-2021-157
Preprint. Discussion started: 7 June 2021

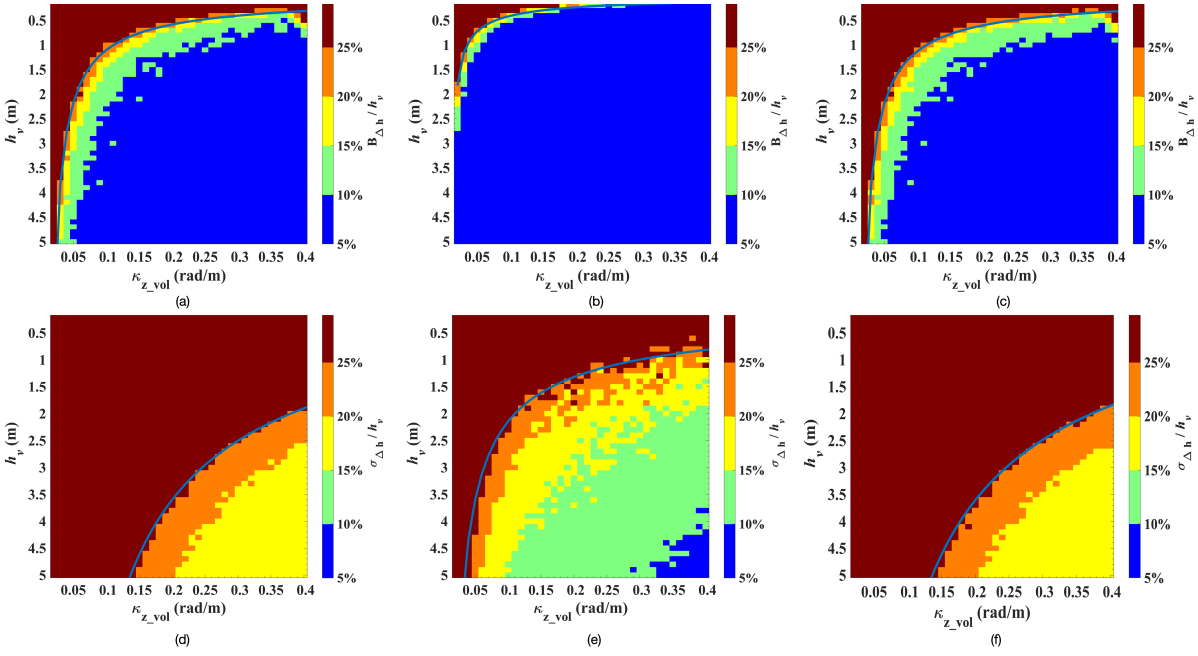

Figure 9. (a)-(c) Relative Bias B_{δ_h}/h_v and (d)-(f) relative standard deviation σ_{δ_h}/h_v of the obtained ice volume h_v for the proposed model. Fixed parameters: $\sigma_1 = 2\,\mathrm{dB/m}$, $m_1 = 0.3$, $z_1 = -0.15\,\mathrm{m}$, $\alpha = 0.5$, variable parameters: (a) and (d) $\sigma_2 = 20\,\mathrm{dB/m}$, $m_2 = 0.5$, (b) and (e) $\sigma_2 = 20\,\mathrm{dB/m}$, $m_2 = 2$, (c) and (f) $\sigma_2 = 100\,\mathrm{dB/m}$, $m_2 = 0.5$. Blue line indicates the threshold of $B_{\delta_h}/h_v = 25\%$ or $\sigma_{\delta_h}/h_v = 25\%$.

($N_s = 10000$) $\tilde{\gamma}_{\mathrm{sim}_i}$ complex samples is generated via Eq. (14) (for magnitude) and Eq. (15) (for phase) with $D = |\tilde{\gamma}_{\mathrm{sim}}|$ and $\beta = \angle\tilde{\gamma}_{\mathrm{sim}}$. Finally, for each simulated $\tilde{\gamma}_{\mathrm{sim}_i}$, the volume height h_{vi} is estimated by the inversion of Eq. 12 with the specific parameters and κ_{z_vol} of the simulation and compared with the input $h_v = z_1 - z_2$ in the first step. The bias $B_{\Delta_h} = |\,\mathbb{E}(h_{vi}) - h_v|$ and the standard deviation $\sigma_{\Delta_h} = \sqrt{\mathbb{E}[(h_{vi} - h_v)^2]}$ are calculated to quantify the estimation accuracy of the model.

By fixing the model parameters $(\sigma_1, \sigma_2, \alpha, m_1, m_2, z_1)$ and varying z_2, B_{Δ_h} and σ_{Δ_h} are functions of volume height $h_v = z_1 - z_2$ and volume-corrected vertical wavenumber κ_{z_vol}. The simulation procedure is performed for h_v ranging from 0 to $5\,\mathrm{m}$ with a step of $0.1\,\mathrm{m}$ and κ_{z_vol} ranging from 0.02 to $0.4\,\mathrm{rad/m}$ at the interval of $0.01\,\mathrm{rad/m}$. The number of looks N is set to be the same value as the experimental data. The bias and the standard deviation relative to volume height are shown in Fig. 9. The plots illustrate that for a specific baseline geometry with a given κ_{z_vol}, the model performance is superior for a certain range of volume height, shown in the blue curve, indicating the 25% threshold, in Fig. 9. For volume heights lower than at the blue curve, the bias and variance are larger than 25%, leading to a lower precision of model inversion. With different σ_2 values, there are no obvious distinctions of B_{Δ_h}/h_v between the Fig. 9(a) and 9(c), as well as σ_{Δ_h}/h_v between Fig. 9(d) and 9(f), respectively. It suggests that the model accuracy is marginally sensitive to ice extinction coefficient σ_2. The layer-to-volume ratio of the bottom layer m_2 plays a key role in model accuracy. From Fig. 9(b) and Fig. 9(e), the B_{Δ_h}/h_v and σ_{Δ_h}/h_v are smaller than those from Fig. 9(a) and Fig. 9(d) due to the larger m_2, indicating the higher model accuracy in this case. The blue curve indicates the 25%-error threshold for both B_{Δ_h}/h_v and σ_{Δ_h}/h_v. It can be a criteria for selecting the best

https://doi.org/10.5194/tc-2021-157
Preprint. Discussion started: 7 June 2021

baseline geometry for the application. For example, with a specific parameter set as Fig. 9(b) and Fig. 9(e), the κ_{z_vol} needs to be larger than $0.40\,\mathrm{rad/m}$ to ensure an effective inversion for ice-volume thickness less than $0.85\,\mathrm{m}$. Since the κ_{z_vol} of the studied SAR image is $0.28\,\mathrm{rad/m}$, in order to achieve an 25%-error accuracy, the ice volume needs to be thicker than $\sim 1.5\,\mathrm{m}$, see Fig. 9(d)-(e). The above assessment also indicates the potential of applying the proposed model to achieve a more accurate result using larger baseline configuration. Note that the baseline should not be too large since it results in stronger interferometric decorrelation which contaminates the topographic information.

4.5 Model simplification

The proposed theoretical model $\tilde{\gamma}_{\mathrm{mod\_T}}$ given in Eq. (12) contains seven parameters: $\sigma_1, \sigma_2, \alpha, m_1, m_2, z_1, z_2$, requiring necessary prior knowledge of the test site. However, such prior knowledge is scarce due to the sparse ground measurement of the Antarctic sea ice, therefore impeding the practical application of the proposed model. As described in Section 4.3, the contributions of the snow volume $\tilde{\gamma}_{\mathrm{v}}(\sigma_1, z_{01})$ and the ice volume $\tilde{\gamma}_{\mathrm{v}}(\sigma_2, z_{12})$ to the theoretical model $\tilde{\gamma}_{\mathrm{mod\_T}}$ show a limited sensitivity for the TanDEM-X acquisition geometry within the investigated range of extinction coefficients σ_1 and σ_2. Additionally, their individual coherence loci are located close to the Dirac delta of the top layer $m_1 e^{i\phi_1}$ in the unit circle. Therefore, the theoretical model can be approximated by merging the contributions of the snow volume, the ice volume, and the top layer into one Dirac delta. This simplified model can be given as

$$\begin{aligned}
&\tilde{\gamma}_{\mathrm{InSAR}'} \\
&= e^{i\phi_0} \frac{\alpha\tilde{\gamma}_{\mathrm{v}}(\sigma_1, z_{01}) + e^{i\phi_1}(1-\alpha)\tilde{\gamma}_{\mathrm{v}}(\sigma_2, z_{12}) + m_1 e^{i\phi_1} + m_2 e^{i\phi_2}}{1 + m_1 + m_2} \\
&\approx e^{i\phi_0} \frac{1 \cdot e^{i\phi_1} + m \cdot e^{i\phi_2}}{1+m} \\
&= e^{i\phi_0} \tilde{\gamma}_{\mathrm{mod_S}}(m, z_1, z_2)
\end{aligned} \tag{16}$$

where $\phi_1 = \kappa_{z\_\mathrm{vol}} z_1$, $\phi_2 = \kappa_{z\_\mathrm{vol}} z_2$, z_1 and z_2 are the position of the top layer and the bottom layer, respectively, and m is the layer-to-layer ratio.

Compared to the theoretical model in Eq. (12), the simplified model in Eq. (16) only has three parameters, remarkably improving the applicability in practice. Figure 10 illustrates the simulations of $\tilde{\gamma}_{\mathrm{mod\_T}}$ and $\tilde{\gamma}_{\mathrm{mod\_S}}$ according to Eq. (12) and Eq. (16), respectively. For $\tilde{\gamma}_{\mathrm{mod\_T}}$, the parameters are set as $\sigma_1 = 2\,\mathrm{dB/m}$, $\sigma_2 = 20\,\mathrm{dB/m}$, $z_1 = -0.15\,\mathrm{m}$, $m_1 = m_2 = 0.5$. For $\tilde{\gamma}_{\mathrm{mod\_S}}$, z_1 is also set to be $-0.15\,\mathrm{m}$, and m varies from 0.3 to 0.4. As we can see, for both coherence magnitude and phase, the simplified model can achieve comparable results to the theoretical model by assuming appropriate m values.

5 Model inversion

In order to apply the proposed simplified model and theoretical model to geophysical parameter retrieval, a methodology is developed for the model inversion. The objective is to estimate the topographic phase ϕ_0 and thus generate the sea ice

https://doi.org/10.5194/tc-2021-157
Preprint. Discussion started: 7 June 2021

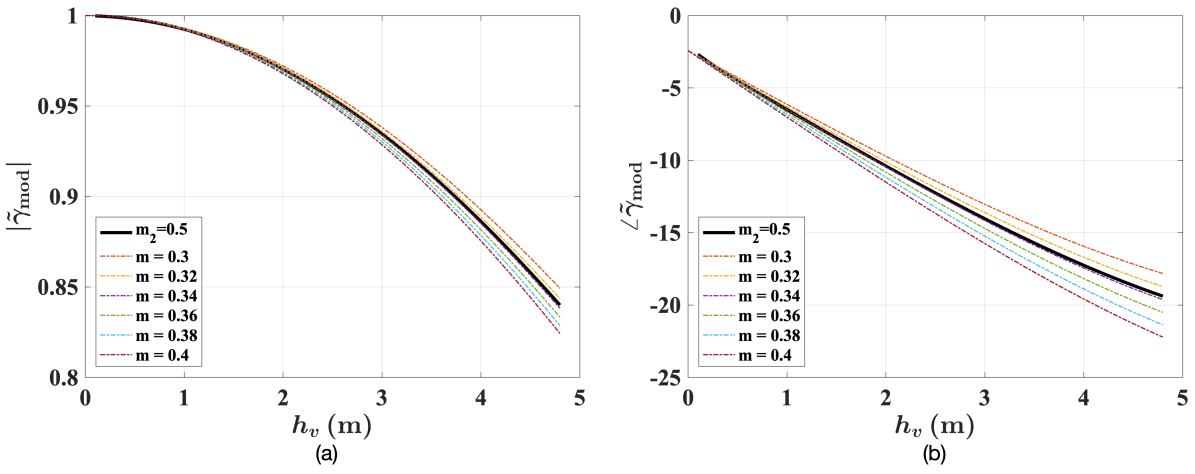

Figure 10. Comparison of complex coherence $\tilde{\gamma}_{\mathrm{mod}}$ from the theoretical model ($\tilde{\gamma}_{\mathrm{mod\_T}}$, thick black line) and the simplified model ($\tilde{\gamma}_{\mathrm{mod\_S}}$, colored lines). (a) Magnitude of the modelled coherence. (b) Phase of the modelled coherence.

topographic height with snow depth for the whole SAR image. The model inversion includes three main steps, illustrated in Fig. 11.

First, for the co-registered data set, the sea ice height (including the snow depth) is measured by the DMS DEM (h_{DMS}). In order to ensure a $\leq 25\%$-error inversion accuracy for a given $\kappa_{z\_\mathrm{vol}} = 0.28\,\mathrm{rad/m}$, only the samples with height above $1.5\,\mathrm{m}$ are selected for processing. As shown in the Step-1 in Fig. 11, the h_{DMS} is converted to phase ϕ_{DMS} via κ_z and used as the prior knowledge. For the simplified model, z_1 is set to be $-0.18\,\mathrm{m}$ according to the snow depth provided by the AMSR-E/AMSR2 Unified Level-3 Daily data set (Meier, W. N., T. Markus, and J. C. Comiso, 2018). The AMSR-E/AMSR2 data set provides snow depth over sea ice values for five day running averages. For the studied area on the campaign date, the averaged snow depth was measured to be $18\,\mathrm{cm}$. For the theoretical model, as discussed in Section 4.3, since the simulated $\tilde{\gamma}_{\mathrm{mod\_T}}$ shows marginal sensitivity to the variance of snow layer extinction coefficient σ_1, ice layer extinction coefficient σ_2, and weight parameter α, these three parameters are fixed to constants. For the snow-covered sea ice of the studied area, the σ_1 and σ_2 are assumed to be $2\,\mathrm{dB/m}$ and $20\,\mathrm{dB/m}$, respectively, referring to the experimental values (Cox and Weeks, 1974; Hallikainen and Winebrenner, 1992). The snow depth z_1 is also set to be $-0.18\,\mathrm{m}$. As for the layer-to-volume ratio of the top layer m_1, the value is set to be 0.3. With above specific parameters, the m_2 (also m for the simplified model) values can be derived by the inversion of the proposed model according to Eq. (12) or Eq. (16) for the theoretical or the simplified model, respectively.

Next, since m_2 or m is the most deterministic parameter in the respective models, the aim is to estimate m_2 or m from the SAR observations (Step-2 in Fig. 11). In addition to interferometry, which provides topographic information, polarimetry reveals information on the scattering processes and is a useful tool to characterize sea ice properties. Among several polarimetric signatures, the co-polarization (coPol) coherence γ_{coPol} is a measurement of the degree of electromagnetic wave depolarization between HH and VV polarizations caused by both the rough surface scattering and the volume scattering (Kasilingam et al.,

https://doi.org/10.5194/tc-2021-157
Preprint. Discussion started: 7 June 2021

The Cryosphere
Discussions
Open Access
EGU

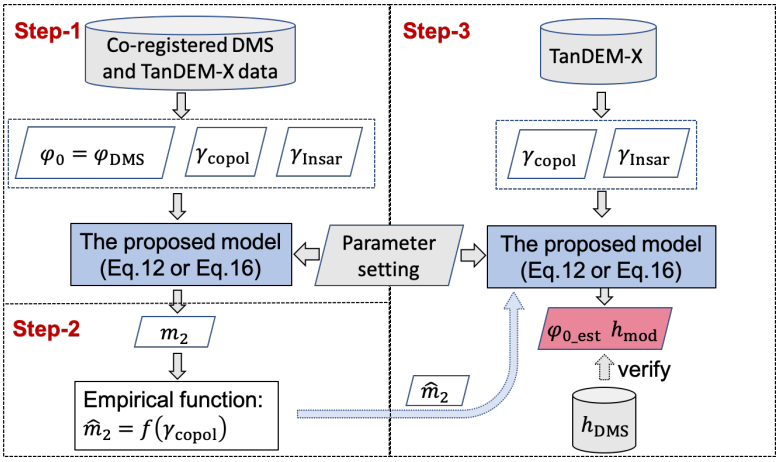

Figure 11. Flow chart of the proposed inversion method.

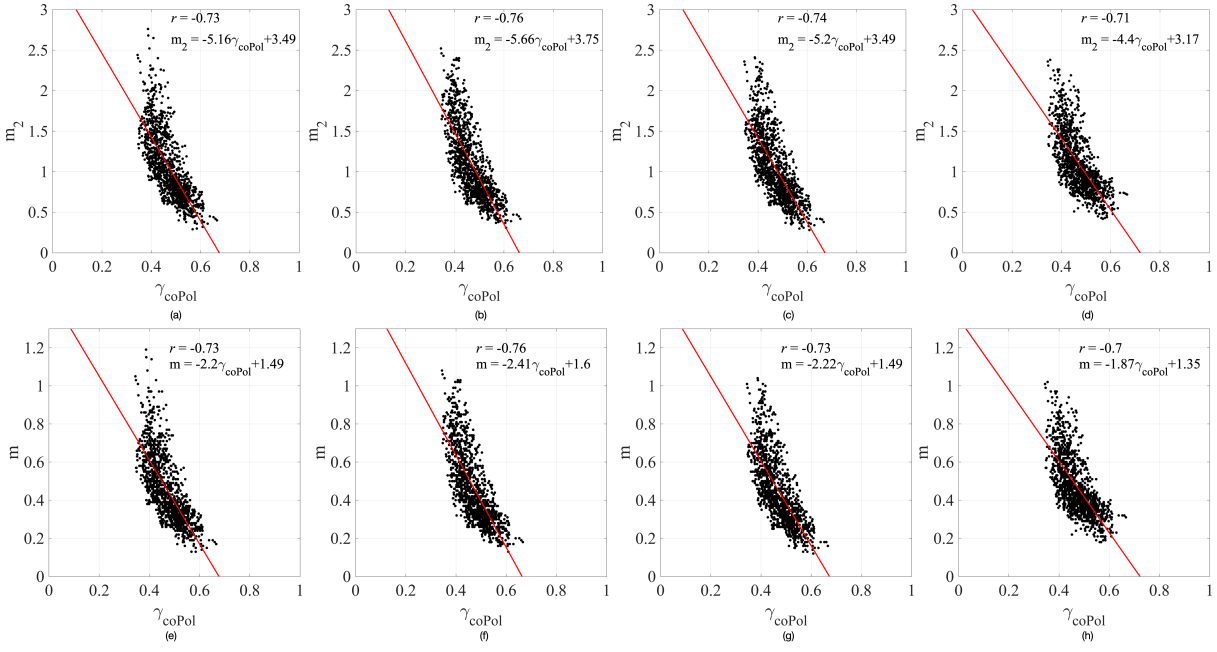

Figure 12. The relation between the bottom-layer layer-to-volume ratio m_2 (respectively m) and the coPol coherence γ_{coPol} for the theoretical model (first row) and the simplified model (second row). (a) and (d) HH polarization, (b) and (f) VV polarization, (c) and (g) Pauli-1: HH+VV polarization, and (d) and (h) Pauli-2: HH-VV polarization. Note the different y-axis scaling for m_2 and m.

https://doi.org/10.5194/tc-2021-157
Preprint. Discussion started: 7 June 2021

2001). γ_{coPol} is demonstrated to be a crucial signature in sea ice characterization (Kim et al., 2011; Wakabayashi et al., 2004; Huang and Hajnsek, 2021). γ_{coPol} can be calculated as (Lee and Pottier, 2009)

$$\tilde{\gamma}_{\mathrm{coPol}} = \gamma_{\mathrm{coPol}} \cdot e^{i\phi_{\mathrm{coPol}}} = \frac{< s_{\mathrm{VV}} s^*_{\mathrm{HH}} >}{\sqrt{< s_{\mathrm{VV}} s^*_{\mathrm{VV}} >< s_{\mathrm{HH}} s^*_{\mathrm{HH}} >}} \tag{17}$$

where s_{HH} and s_{VV} are single look complex images in HH and VV polarization, respectively. The symbol $< . >$ denotes an ensemble average. A 4×12 window in azimuth and slant range is applied to estimate γ_{coPol}. It is found that m_2 (also m) is inversely related to γ_{coPol} for the four polarizations, shown in Fig. 12, enlightening us to derive an empirical function between the parameter m_2 (also m) and γ_{coPol}. As shown in Step-2 in Fig. 11, the linear functions for the different polarizations are derived by least-squares fitting and are detailed in Fig. 12. Note the almost identical correlation coefficients of the fitted linear function for the theoretical model (first row) and the simplified model (second row) in Fig. 12. This underlines that the theoretical model can be approximated by the simplified model. The parameters of the linear functions for m_2 and m are of course different. Then, the fitted functions are applied to estimate $\hat{m}_2$ (also $\hat{m}$), which will be used as an input to perform the model inversion for the whole image, including the area without DMS measurements.

Finally, as shown in the Step-3 in Fig. 11, for the TanDEM-X data without the prior knowledge of DMS measurement, the γ_{coPol} together with the derived linear function is utilized to estimate $\hat{m}_2$ (also $\hat{m}$) for each pixel. With the specific parameter setting, the estimated $\hat{m}_2$ (also $\hat{m}$), and the $\tilde{\gamma}_{\mathrm{InSAR}'}$ from InSAR pairs, the topographic phase ϕ_{0_est} can be retrieved by solving Eq. (12) or Eq. (16), and then converted to height h_{mod} in meter via κ_z. The area overlaid by the DMS flight track is used to verify the model-inversion result quantitatively and visually, which will be illustrated in the next section.

6 Experimental results

In this section, the proposed two-layer plus volume model and its simplified version are inverted to estimate sea ice topography following the developed scheme. Note that the retrieved sea ice topography refers to the sea ice height including the snow depth above the local sea level. Both visual and quantitative analyses are given to evaluate the retrieval performance.

6.1 Retrieval performance of the simplified model

The sea ice topographic retrievals based on the simplified model (Fig. 11) are performed for the four polarizations (HH, VV, Pauli-1, and Pauli-2), respectively. Because of the marginal visual distinction among polarizations, only the HH-polarization result is presented for conciseness, while the conclusion is equivalent for all four polarizations. The quantitative evaluation is given for the four polarizations.

The model-retrieved sea ice topography in HH polarization is shown in Fig. 13. The strip between the grey lines is the area covered by the DMS DEM which is superimposed on the model-retrieved result with the same colormap. In general, the retrieved height varies from 0 to $3\,\mathrm{m}$ for the whole image, showing a good agreement with the height range obtained by DMS measurements. Three areas are selected and enlarged for detailed analyses. Figure 13(b) is the zoom-in of Area 1, where several sea ice areas are higher than $2.5\,\mathrm{m}$. The model-retrieved height (outside the grey lines) shows good continuity with the

https://doi.org/10.5194/tc-2021-157
Preprint. Discussion started: 7 June 2021

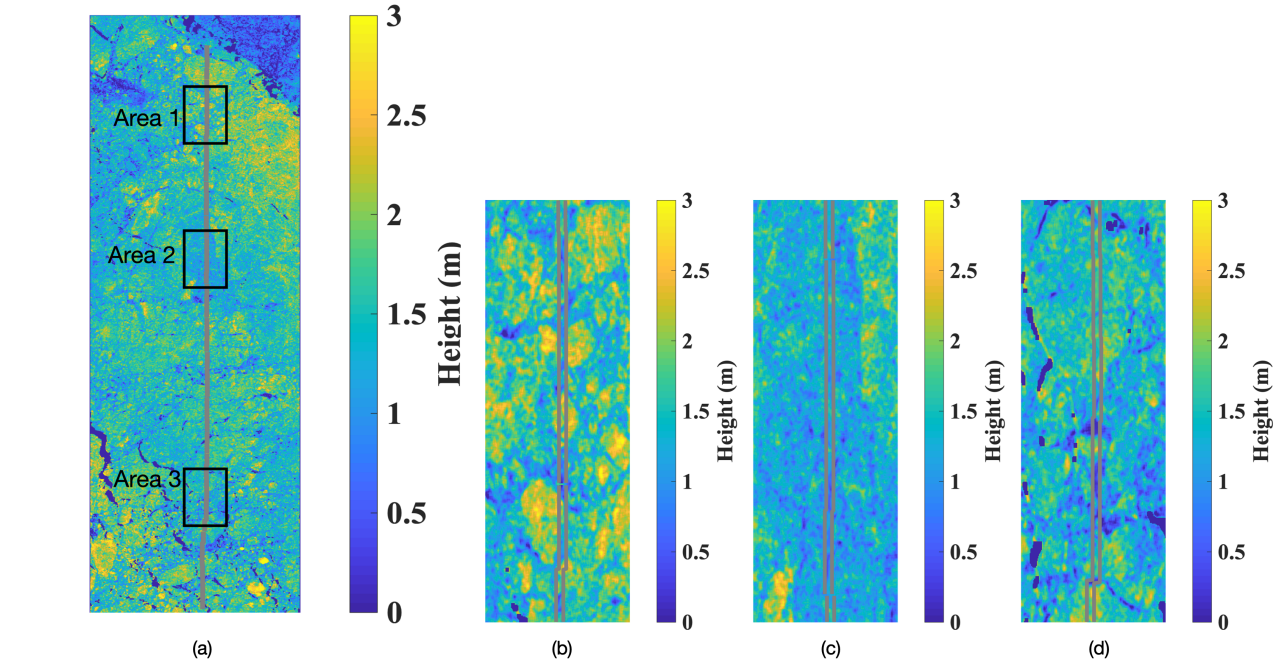

Figure 13. Sea ice topographic retrieval from the proposed method. The transect from the DMS DEM is plotted between grey lines. (a) The whole studied SAR image. (b)-(d) Zoom-in of Areas 1-3.

DMS measurements (between the grey lines), indicating the effectiveness of the proposed method. Area 2 is mainly covered with ice lower than $2\,\mathrm{m}$. The sea ice topographic retrieval of Area 2 is shown in Fig. 13(c), where the consistency between the model-retrieved Pol-InSAR DEM and the DMS DEM is again visually verified. Area 3 (Fig. 13(d)), including sea ice in the range of $2-2.5\,\mathrm{m}$, shows the preservation of continuous sea ice features as well. Therefore, from the qualitative comparison, the model-retrieved Pol-InSAR DEM demonstrates a good visual agreement with the DMS DEM.

The comparison of the height profiles in HH polarization along the DMS strip is shown in Fig. 14(a). The model-retrieved DEM h_{Model} and the DMS DEM h_{DMS} along the transect are plotted in the red and blue line, respectively. Since we only select the samples with height above $1.5\,\mathrm{m}$, the grey sections indicate the removed samples which are not considered in the experiment. As observed from Fig. 14(a), the model-retrieved height has, in general, a good capture of the topographic variation. The height difference ($h_{\mathrm{diff\_S}}$) between the h_{DMS} and the simplified model-retrieved height is shown in Fig. 14(b) (blue). Compared with the larger height difference ($h_{\mathrm{diff\_ori}}$) between the h_{DMS} and the initial InSAR DEM in Fig. 14(b) (green), the surface-elevation bias is properly compensated by using the simplified model. In the HH polarization, the $RMSE$ of the model-retrieved height is $\sim 0.22\,\mathrm{m}$ relative to the DMS DEM. Compared to the original InSAR-derived height with $RMSE = 1.02\,\mathrm{m}$, Fig. 14(a) reveals the pronounced improvement of applying the proposed model to estimate sea ice topographic height, considering that the $RMSE$ in the DMS DEM is already $0.2\,\mathrm{m}$ to start with (Dotson and Arvesen., 2012, updated 2014).

https://doi.org/10.5194/tc-2021-157
Preprint. Discussion started: 7 June 2021

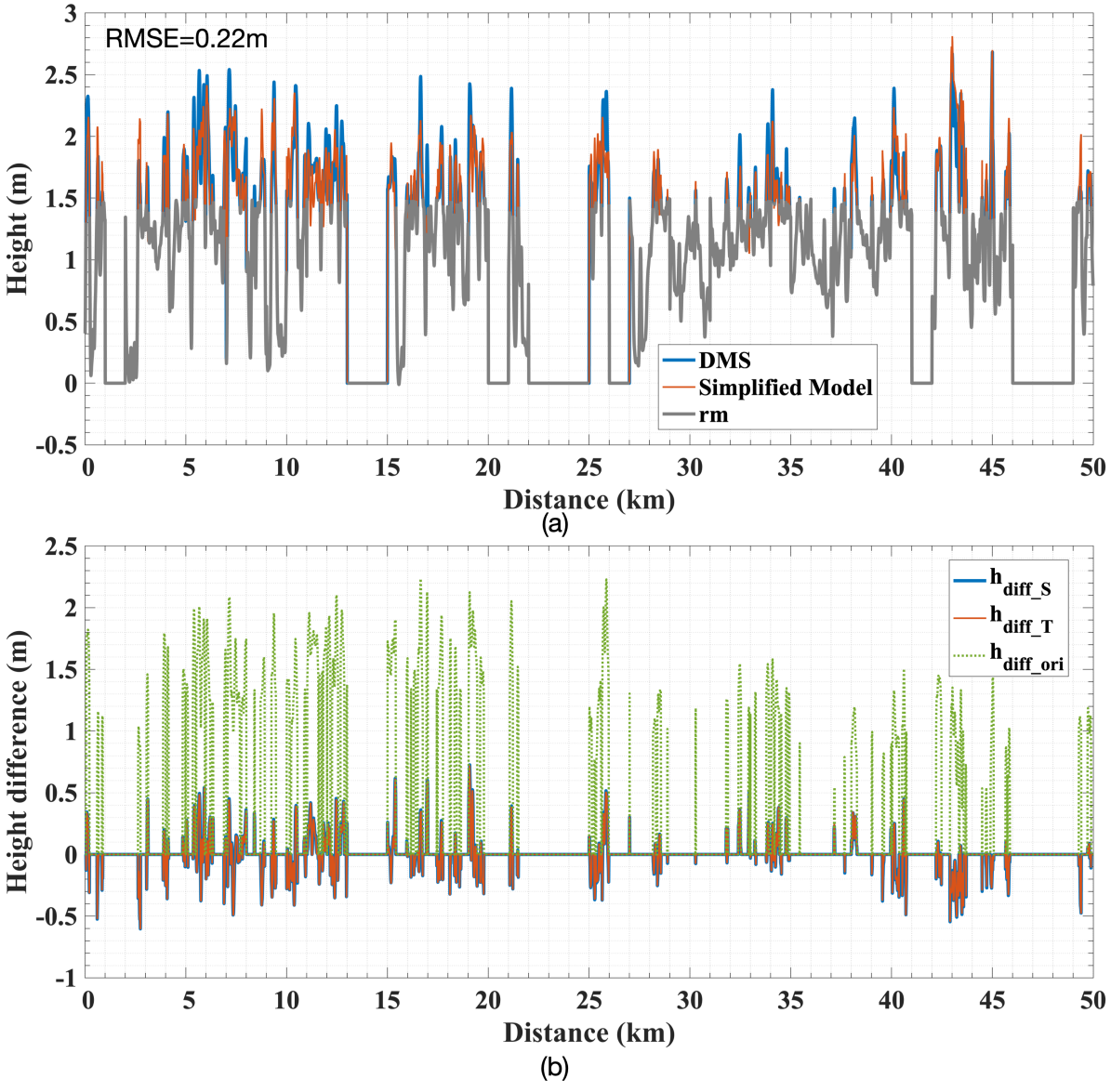

Figure 14. (a) Sea ice height profiles from DMS measurement (blue) and model (red) excluding the removed sections (grey). (b) Height difference between the DMS measurement and the simplified model-derived height (blue), theoretical model-derived height (red), or original InSAR-derived height (green).

https://doi.org/10.5194/tc-2021-157
Preprint. Discussion started: 7 June 2021


The Cryosphere Discussions
Open Access
EGU

Table 1. The $RMSE$ of model-retrieved height h_{Model} for the four polarizations.

Polarization	HH	VV	Pauli-1	Pauli-2
The InSAR method $RMSE(\mathrm{m})$	1.0156	1.0179	1.0103	1.0484
The simplified model $RMSE(\mathrm{m})$	0.2227	0.2240	0.2205	0.2679
The theoretical model $RMSE(\mathrm{m})$	0.2228	0.2246	0.2209	0.2665

The third row in Table 1 summarizes the performances between h_{Model} and h_{DMS} for the four polarizations. The $RMSE$ values across the four polarizations are similar, ranging from $0.22\,\mathrm{m}$ to $0.27\,\mathrm{m}$. The larger $RMSE$ values in the Pauli-2 channel could result from the lower SNR values. The polarization-independent performances further reveal the inherent property of the studied sea ice to be a polarization-independent volume among co-pol channels in X-band radar frequencies.

6.2 Retrieval performance of the theoretical model

For the theoretical model which requires necessary prior knowledge (e.g., snow density, ice salinity, air temperature) to determine the input parameters, the inversion performance depends on the study area and the sea ice structural characteristics. In this section, the inversion of the theoretical model is achieved by fixing parameters which have marginal effects on the model predictions and by estimating the layer-to-volume ratio of the bottom layer from a polarimetric signature: The coPol coherence. With the specific parameter set assumed in Section 5, the theoretical model is inverted according to the proposed method (Fig. 11) to retrieve the sea ice topography. The height difference ($h_{\mathrm{diff\_T}}$) between the h_{DMS} and the theoretical model-retrieved height is shown in Fig. 14(b) (red), visualizing the similar performance of the theoretical and the simplified model. The results also show that the retrieval accuracy in terms of $RMSE$ (the forth row in Table 1) of the theoretical model is almost identical to the simplified model, just slightly different in the fourth digits after the decimal point. It demonstrates that the theoretical model can well correct the penetration-bias of InSAR signals and achieve an effective sea ice height retrieval from dual-pol single-pass interferometric data, fulfilling the primary goal of this study.

The comparable performance between the theoretical and simplified model on the studied area convinces the effectiveness of employing the simplified model to achieve an accurate sea ice topographic retrieval. In the cases when the ground measurements are sparse, the simplified model requires only one parameter (i.e., snow depth over sea ice), significantly reducing the model complexity and improving the applicability in practice.

6.3 Discussion on model complexity and observation space

The proposed two-layer plus volume model inherently includes seven parameters with the assumption of their independence of polarization. In the case of a polarization-dependent volume, two more parameters are introduced for each volume and

https://doi.org/10.5194/tc-2021-157
Preprint. Discussion started: 7 June 2021

thus further complicate the inversion. In order to achieve the model inversion, one method is to develop a simplified model as presented in Section 6.1, which accurately approximates the behavior of the theoretical model and requires only the snow depth as an input parameter. Another method to achieve the theoretical model inversion is to increase the observation space to full polarization and/or multi-baseline configurations. Acquisitions of full-pol data improve the inversion capability over single-pol or dual-pol configurations. For instance, dual-baseline quad-pol data provide 12 independent observables and thereby offer an opportunity to theoretically invert a model with a maximum of 12 parameters. In Section 4.4, we have illustrated the theoretical performance of the proposed model with various baseline configurations (κ_z) and obtained a certain range which can ensure high inversion accuracy. It reveals the potential to establish an inversion scheme by combining observations from a range of different κ_z, where larger baselines respectively larger κ_z values are expected to improve the retrieval accuracy. With quad-pol and multi-baseline data acquired over sea ice in the future, developing a refined inversion scheme for more diverse scattering scenarios and thinner sea ice heights will be promising.

7 Conclusions

In this study, the potential to retrieve sea ice topography with the Pol-InSAR technique was validated with single-pass interferometric SAR data and airborne photogrammetric measurements over the thick and deformed sea ice with snow cover in the west Weddell sea. The DMS DEM reveals that the sea ice topography along the flight track varies from 0 to $2.68\,\mathrm{m}$ with the average height being $1.27\,\mathrm{m}$. The average elevation difference between the conventional InSAR DEM and the DMS DEM is $\sim 1\,\mathrm{m}$ in the four investigated polarizations (HH, VV, Pauli-1, and Pauli-2), suggesting the demand for a valid method to obtain sea ice topography and to correct for the penetration of the microwave signals into the sea ice. By exploiting the interferometric coherence, a two-layer plus volume model was proposed to characterize the sea ice vertical scattering structure and an inversion scheme was developed for height retrieval. The model's theoretical accuracy was assessed for various vertical wavenumber values, yielding a threshold of $1.5\,\mathrm{m}$ volume thickness to ensure 25% accuracy at the employed baseline configuration with $\kappa_z = 0.28\,\mathrm{rad/m}$. The assessment also showed the potential to apply the model to multi-baseline configurations, giving the ability to adjust a sensor to the particular type of sea ice. For instance a configuration with $\kappa_z = 0.40\,\mathrm{rad/m}$ ensures an effective inversion for ice-volume thickness less than $0.85\,\mathrm{m}$.

The proposed theoretical model requires seven input parameters depending on the environmental conditions over the test site, which are unavailable in many practical applications. In order to reduce the model complexity and improve the model feasibility in practical applications, a simplified model requiring only the input of snow depth was proposed based on the analyses of the model sensitivity to different parameterizations. For the theoretical and simplified model, the layer-to-volume ratio of the bottom layer, respectively the layer-to-layer ratio, were observed to be inversely correlated to an essential polarimetric signature: the coPol coherence. This relationship was exploited in the inversion scheme by estimating those parameters from the coPol coherence with a fitted linear function. Note that the empirical relation in this study was derived over a specific area with snow-covered deformed ice; therefore it is not an independent method that can be directly applied to wider sea ice areas including various ice types. With more co-registered data acquired from SAR and reference DEM in the future, how to extend

https://doi.org/10.5194/tc-2021-157
Preprint. Discussion started: 7 June 2021

this empirical relation to wider acquisition areas from the same TanDEM-X configuration and regions covered by different sea ice types are worthy of further investigation.

The effectiveness of both the theoretical and simplified models and the proposed inversion scheme were verified with the DMS measurements for the sea ice height above $1.5\,\mathrm{m}$. The model-retrieved sea ice topography achieved a $RMSE$ as low as $0.22\,\mathrm{m}$, which is significantly better than the conventional InSAR DEM. This indicates the capability to correct for the microwave signal penetration depth and to generate a precise wide-swath topographic map from dual-pol single-pass InSAR data. The polarization-independent volume property of sea ice in the co-pol channels in X-band radar frequency, which was concluded from the similar retrieval performance across polarizations, gave insights to develop superior models for height retrieval in the future. Next work will include investigating the possibility of sea ice topographic retrieval for various types of sea ice, such as thin ice and newly formed ice.

Data availability. TanDEM-X data can be obtained from the German Aerospace Center (DLR) and downloaded on the website (https://eoweb.dlr.de). DMS data can be obtained from the National Snow and Ice Data Center and downloaded on the website (https://nsidc.org/data/icebridge)

Author contributions. LH conducted the PolInSAR processing and modelling. GF and IH provided valuable comments on all aspects of the modelling and experiments. LH drafted the initial manuscript, and all co-authors contributed to the improvements of the text.

Competing interests. The authors declare that they have no conflict of interest.

Acknowledgements. The authors would like to thank everyone involved in the OTASC campaign, which was conducted by DLR and NASA.

https://doi.org/10.5194/tc-2021-157
Preprint. Discussion started: 7 June 2021

References

Abdalati, W., Zwally, H. J., Bindschadler, R., Csatho, B., Farrell, S. L., Fricker, H. A., Harding, D., Kwok, R., Lefsky, M., Markus, T., et al.: The ICESat-2 laser altimetry mission, Proceedings of the IEEE, 98, 735–751, https://doi.org/10.1109/JPROC.2009.2034765, 2010.

Albert, M. D., Lee, Y. J., Ewe, H.-T., and Chuah, H.-T.: Multilayer model formulation and analysis of radar backscattering from sea ice, Progress in Electromagnetics Research, 128, 267–290, https://doi.org/10.2528/PIER12020205, 2012.

Castellani, G., Lüpkes, C., Hendricks, S., and Gerdes, R.: Variability of Arctic sea-ice topography and its impact on the atmospheric surface drag, J. Geophys. Res.: Oceans, 119, 6743–6762, https://doi.org/10.1002/2013JC009712, 2014.

Cloude, S.: Polarisation: applications in remote sensing, Oxford University Press, https://doi.org/10.1093/acprof:oso/9780199569731.001.0001, 2010.

Cox, G. F. and Weeks, W. F.: Salinity variations in sea ice, J. Glaciol., 13, 109–120, https://doi.org/10.1017/S0022143000023418, 1974.

Dall, J.: InSAR elevation bias caused by penetration into uniform volumes, IEEE Trans. Geosci. Remote Sens., 45, 2319–2324, https://doi.org/10.1109/TGRS.2007.896613, 2007.

Dammann, D. O., Eriksson, L. E. B., Nghiem, S. V., Pettit, E. C., Kurtz, N. T., Sonntag, J. G., Busche, T. E., Meyer, F. J., and Mahoney, A. R.: Iceberg topography and volume classification using TanDEM-X interferometry, The Cryosphere, 13, 1861–1875, https://doi.org/10.5194/tc-13-1861-2019, 2019.

Dierking, W.: Laser profiling of the ice surface topography during the Winter Weddell Gyre Study 1992, J. Geophys. Res.: Oceans, 100, 4807–4820, https://doi.org/10.1029/94JC01938, 1995.

Dierking, W., Lang, O., and Busche, T.: Sea ice local surface topography from single-pass satellite InSAR measurements: a feasibility study, The Cryosphere, 11, 1967–1985, https://doi.org/10.5194/tc-11-1967-2017, 2017.

Divine, D. V., Pedersen, C. A., Karlsen, T. I., Aas, H. F., Granskog, M. A., Hudson, S. R., and Gerland, S.: Photogrammetric retrieval and analysis of small scale sea ice topography during summer melt, Cold Reg. Sci. Technol., 129, 77–84, https://doi.org/10.1016/j.coldregions.2016.06.006, 2016.

Dominguez, R.: IceBridge DMS L1B Geolocated and Orthorectified Images, Version 1, Boulder, Colorado USA: NASA National Snow and Ice Data Center Distributed Active Archive Center, https://doi.org/10.5067/OZ6VNOPMPRJ0. Accessed Nov 22, 2018., 2010, updated 2018.

Dotson, R. and Arvesen., J.: IceBridge DMS L3 Photogrammetric DEM, Version 1., Boulder, Colorado USA: NASA National Snow and Ice Data Center Distributed Active Archive Center, https://doi.org/10.5067/39YO5T544XCC. Accessed Nov 22, 2018., 2012, updated 2014.

Duque, S., Balss, U., Rossi, C., Fritz, T., and Balzer, W.: TanDEM-X payload ground segment, CoSSC generation and interferometric considerations, German Aerospace Center: Oberpfaffenhofen, Germany, https://tandemx-science.dlr.de/pdfs/TD-PGS-TN-3129_CoSSCGenerationInterferometricConsiderations_1.0.pdf, 2012.

Eineder, M., Fritz, T., Mittermayer, J., Roth, A., Boerner, E., and Breit, H.: TerraSAR-X ground segment, basic product specification document, Tech. rep., Cluster Applied Remote Sensing (CAF) Oberpfaffenhofen (Germany), 2008.

Farrell, S. L., Markus, T., Kwok, R., and Connor, L.: Laser altimetry sampling strategies over sea ice, Ann. Glaciol., 52, 69–76, https://doi.org/10.3189/172756411795931660, 2011.

Fischer, G., Papathanassiou, K. P., and Hajnsek, I.: Modeling multifrequency Pol-InSAR data from the percolation zone of the Greenland Ice Sheet, IEEE Trans. Geosci. Remote Sens., 57, 1963–1976, https://doi.org/10.1109/TGRS.2018.2870301, 2018.

Garbrecht, T., Lüpkes, C., Hartmann, J., and Wolff, M.: Atmospheric drag coefficients over sea ice–validation of a parameterisation concept, Tellus A: Dyn. Meteorol. Oceanogr., 54, 205–219, https://doi.org/10.3402/tellusa.v54i2.12129, 2002.

Goldstein, R. M. and Werner, C. L.: Radar interferogram filtering for geophysical applications, Geophys. Res. Lett., 25, 4035–4038, https://doi.org/10.1029/1998GL900033, 1998.

Goldstein, R. M., Zebker, H. A., and Werner, C. L.: Satellite radar interferometry: Two-dimensional phase unwrapping, Radio Sci., 23, 713–720, https://doi.org/10.1029/RS023i004p00713, 1988.

Hallikainen, M. and Winebrenner, D. P.: The physical basis for sea ice remote sensing, Microwave remote sensing of sea ice, 68, 29–46, https://doi.org/10.1029/GM068p0029, 1992.

Haykin, S., Lewis, E. O., Raney, R. K., and Rossiter, J. R.: Remote sensing of sea ice and icebergs, vol. 13, John Wiley & Sons, 1994.

Huang, L. and Hajnsek, I.: Polarimetric Behaviour for the Derivation of Sea Ice Topographic Height from TanDEM-X Interferometric SAR Data, IEEE J. Sel. Top. Appl. Earth Obs. Remote Sens., 14, 1095–1110, https://doi.org/10.1109/JSTARS.2020.3036395, 2021.

Joerg, H., Pardini, M., Hajnsek, I., and Papathanassiou, K. P.: 3-D Scattering Characterization of Agricultural Crops at C-Band Using SAR Tomography, IEEE Trans. Geosci. Remote Sens., 56, 3976–3989, https://doi.org/10.1109/TGRS.2018.2818440, 2018.

Kasilingam, D., Schuler, D., and Lee, J.-S.: The depolarization of radar backscatter from rough surfaces due to surface roughness and slopes, in: Proc. IGARSS., vol. 2, pp. 925–927, IEEE, https://doi.org/10.1109/IGARSS.2001.976682, 2001.

Kim, J.-W., Kim, D.-j., and Hwang, B. J.: Characterization of Arctic sea ice thickness using high-resolution spaceborne polarimetric SAR data, IEEE Trans. Geosci. Remote Sens., 50, 13–22, https://doi.org/10.1109/TGRS.2011.2160070, 2011.

Krieger, G., Moreira, A., Fiedler, H., Hajnsek, I., Werner, M., Younis, M., and Zink, M.: TanDEM-X: A satellite formation for high-resolution SAR interferometry, IEEE Trans. Geosci. Remote Sens., 45, 3317–3341, https://doi.org/10.1109/TGRS.2007.900693, 2007.

Kugler, F., Lee, S.-K., Hajnsek, I., and Papathanassiou, K. P.: Forest height estimation by means of Pol-InSAR data inversion: The role of the vertical wavenumber, IEEE Trans. Geosci. Remote Sens., 53, 5294–5311, https://doi.org/10.1109/TGRS.2015.2420996, 2015.

Lee, J.-S. and Pottier, E.: Polarimetric radar imaging: from basics to applications, CRC press, https://doi.org/10.1080/01431161.2010.519925, 2009.

Leinss, S.: Depth, anisotropy, and water equivalent of snow estimated by radar interferometry and polarimetry, Ph.D. thesis, ETH Zurich, https://doi.org/10.3929/ethz-a-010603517, 2015.

Lopes, A., Mougin, E., Beaudoin, A., Goze, S., Nezry, E., Touzi, R., Karam, M., and Fung, A.: Phase difference statistics related to sensor and forest parameters, in: Proc. IGARSS., pp. 779–781, https://doi.org/10.1109/IGARSS.1992.576832, 1992.

Meier, W. N., T. Markus, and J. C. Comiso: AMSR-E/AMSR2 Unified L3 Daily 12.5 km Brightness Temperatures, Sea Ice Concentration, Motion & Snow Depth Polar Grids, Version 1, Boulder, Colorado USA: NASA National Snow and Ice Data Center Distributed Active Archive Center, https://doi.org/10.5067/RA1MIJOYPK3P. Accessed Jan 23, 2021., 2018.

Nghiem, S., Borgeaud, M., Kong, J., and Shin, R.: Polarimetric remote sensing of geophysical media with layer random medium model, Progress in Electromagnetics Research, 3, 1–73, https://doi.org/10.1007/978-1-4899-3677-6_50, 1990.

Nghiem, S., Kwok, R., Yueh, S., and Drinkwater, M.: Polarimetric signatures of sea ice: 1. Theoretical model, J. Geophys. Res.: Oceans, 100, 13 665–13 679, https://doi.org/10.1029/95JC00937, 1995a.

Nghiem, S., Kwok, R., Yueh, S., and Drinkwater, M.: Polarimetric signatures of sea ice: 2. Experimental observations, J. Geophys. Res.: Oceans, 100, 13 681–13 698, https://doi.org/10.1029/95JC00938, 1995b.

https://doi.org/10.5194/tc-2021-157
Preprint. Discussion started: 7 June 2021

Nghiem, S., Busche, T., Kraus, T., Bachmann, M., Kurtz, N., Sonntag, J., Woods, J., Ackley, S., Xie, H., Maksym, T., et al.: Remote Sensing of Antarctic Sea Ice with Coordinated Aircraft and Satellite Data Acquisitions, in: Proc. IGARSS., pp. 8531–8534, IEEE, https://doi.org/10.1109/IGARSS.2018.8518550, 2018.

Papathanassiou, K. P. and Cloude, S. R.: Single-baseline polarimetric SAR interferometry, IEEE Trans. Geosci. Remote Sens., 39, 2352–2363, https://doi.org/10.1109/36.964971, 2001.

Petty, A. A., Tsamados, M. C., Kurtz, N. T., Farrell, S. L., Newman, T., Harbeck, J. P., Feltham, D. L., and Richter-Menge, J. A.: Characterizing Arctic sea ice topography using high-resolution IceBridge data, The Cryosphere, 10, 1161–1179, https://doi.org/10.5194/tc-10-1161-2016, 2016.

Rampal, P., Weiss, J., and Marsan, D.: Positive trend in the mean speed and deformation rate of Arctic sea ice, 1979–2007, J. Geophys. Res.: Oceans, 114, https://doi.org/10.1029/2008JC005066, 2009.

Rodriguez, E. and Martin, J.: Theory and design of interferometric synthetic aperture radars, in: IEE Proceedings F (Radar and Signal Processing), vol. 139, pp. 147–159, IET, https://doi.org/10.1049/ip-f-2.1992.0018, 1992.

Schutz, B. E., Zwally, H. J., Shuman, C. A., Hancock, D., and DiMarzio, J. P.: Overview of the ICESat mission, Geophys. Res. Lett., 32, https://doi.org/10.1029/2005GL02400, 2005.

Sharma, J. J., Hajnsek, I., Papathanassiou, K. P., and Moreira, A.: Estimation of glacier ice extinction using long-wavelength airborne Pol-InSAR, IEEE Trans. Geosci. Remote Sens., 51, 3715–3732, https://doi.org/10.1109/TGRS.2012.2220855, 2012.

Touzi, R. and Lopes, A.: Statistics of the Stokes parameters and of the complex coherence parameters in one-look and multilook speckle fields, IEEE Trans. Geosci. Remote Sens., 34, 519–531, https://doi.org/10.1109/36.485128, 1996.

Toyota, T., Massom, R., Tateyama, K., Tamura, T., and Fraser, A.: Properties of snow overlying the sea ice off East Antarctica in late winter, 2007, Deep Sea Res. Part II, 58, 1137–1148, https://doi.org/10.1016/j.dsr2.2010.12.002, 2011.

Tucker, W. B., Sodhi, D. S., and Govoni, J. W.: Structure of first-year pressure ridge sails in the Prudhoe Bay region, in: The Alaskan Beaufort Sea, edited by Barnes, P. W., Schell, D. M., and Reimnitz, E., pp. 115–135, Academic Press, https://doi.org/https://doi.org/10.1016/B978-0-12-079030-2.50012-5, 1984.

Tucker III, W. and Govoni, J.: Morphological investigations of first-year sea ice pressure ridge sails, Cold Reg. Sci. Technol., 5, 1–12, https://doi.org/10.1016/0165-232X(81)90036-7, 1981.

Wakabayashi, H., Matsuoka, T., Nakamura, K., and Nishio, F.: Polarimetric characteristics of sea ice in the sea of Okhotsk observed by airborne L-band SAR, IEEE Trans. Geosci. Remote Sens., 42, 2412–2425, https://doi.org/10.1109/TGRS.2004.836259, 2004.

Yitayew, T. G., Dierking, W., Divine, D. V., Eltoft, T., Ferro-Famil, L., Rösel, A., and Negrel, J.: Validation of Sea-Ice Topographic Heights Derived From TanDEM-X Interferometric SAR Data With Results From Laser Profiler and Photogrammetry, IEEE Trans. Geosci. Remote Sens., 56, 6504–6520, https://doi.org/10.1109/TGRS.2018.2839590, 2018.